Engineering Structures 124 (2016) 521–538

Contents lists available at ScienceDirect

Engineering Structures

journal homepage: www.elsevier.com/locate/engstruct

A nonlinear quadrilateral layered membrane element with drilling degrees of freedom for the modeling of reinforced concrete walls

F. Rojas [a,*], J.C. Anderson [b], L.M. Massone [a]

[a] Department of Civil Engineering, University of Chile, Av. Blanco Encalada 2002, Santiago, Chile
[b] Department of Civil and Environmental Engineering, University of Southern California, 3620 S. Vermont Av., Los Angeles, CA 90089, USA

ARTICLE INFO

Article history:
Received 26 February 2016
Revised 20 May 2016
Accepted 17 June 2016
Available online 6 July 2016

Keywords:
Reinforced concrete walls
Smeared orthotropic concrete material
Smeared steel reinforcement
Membrane element with drilling degrees of freedom

ABSTRACT

In this article, the formulation and verification of a nonlinear quadrilateral layered membrane element with drilling degrees of freedom for the nonlinear analysis of reinforced concrete (RC) walls under static and cycling loads are presented. The formulation is based on a quadrilateral element with twelve degrees of freedom (DOF), two displacements and one drilling DOF per node, which is defined by a blended field interpolation for the displacements over the element, and a layered system for the element section consisting of fully bonded, smeared steel reinforcement and smeared orthotropic concrete material with a rotating angle formulation, and a stiffness tangent approach. The drilling DOF refers to the incorporation of the in-plane rotation as a DOF at each element node. The blended field interpolation has the advantage of producing a smoother strain distribution inside each element, which facilitates element convergence, and the layered section formulation allows for the properties of the concrete and steel over the thickness of the wall to be modified to properly represent the different wall components, such as the concrete cover, steel rebar and confined concrete. Additionally, the formulation introduces a rotational DOF at each node, which allows the membranes to connect directly to beam and column elements. Moreover, this formulation incorporates the coupling of axial, flexural and shear behavior observed on the different configurations of RC wall structures. To verify this formulation, the results of a set of available experimental data reported in the literature for RC wall elements, with different configurations (slender walls, squat walls, wall with irregular disposition of openings) and levels of confinement, under monotonic and reversed loads are compared with the results obtained from the corresponding analytical model. The formulation is notably consistent with the experimental data and can predict the maximum capacity, the global (force vs deformation) and local responses (strain along the wall) and incorporate the coupling of axial, flexural and shear behavior observed in the different configurations of RC wall structures.

1. Introduction

Although the design of RC walls is a relatively simple procedure when using current codes, the behavior of RC walls is actually highly complex because they behave differently depending on their configuration (wall size, height/length ratio, steel reinforcement, etc.) and loading conditions. This scenario implies that the behavior of RC walls depends on the interrelation and coupling of a combination of flexural, shear, and axial deformation over their cross-sections at different levels, along with other complex mechanisms such as rigid body rotation for the bond slippage of the longitudinal reinforcement at the base of the wall, effects of confinement, dowel action in reinforcement, cracking, aggregate interlock, creep, and tension stiffening, which have been demonstrated by various researchers [1–4].

For example, the walls used in mid- to high-rise buildings exhibit mainly flexural behavior, with the deformation concentrated at the larger moment, typically near the ground level. Failure in this type of wall is characterized by horizontal cracks at the edges of the wall. In low-rise buildings, however, the walls behave primarily in shear, and diagonal cracks are produced. These main behaviors typically occur in isolated walls. Once these walls are combined with other elements or walls in the building, the behavior can change, producing combinations of flexural, compression and shear failure. Such behavior has been described in the reports of the Reconnaissance team of the Los Angeles Tall Building Structural Design Council [5–8] and of the ERRI Reconnaissance team [9] after the recent Chilean earthquake. Because of this

* Corresponding author.
E-mail addresses: frojas@ing.uchile.cl (F. Rojas), jamesa@usc.edu (J.C. Anderson), lmassone@ing.uchile.cl (L.M. Massone).

http://dx.doi.org/10.1016/j.engstruct.2016.06.024
0141-0296/

complex behavior in RC walls, a large amount of research and experimentation in recent decades has been dedicated to providing enough data to represent the walls and develop analytical models that can accurately predict their behavior and important material characteristics, such as concrete stiffening, cracking, bond slippage and vertical strain distribution along the walls.

Typically, analytical models can be separated into two main groups, macroscopic models and microscopic models. Macroscopic models are based on predicting the overall behavior of a wall element using simplified assumptions and idealizations [10]. This process is typically carried out by creating a system of springs, in which each spring has an independent hysteric curve that represents a portion of the wall's behavior. Examples of such systems include the multi-component-in-parallel model or multi-vertical-line-element model and the truss-type model. The multi-vertical-line-element model, or fiber-based model, is characterized by the combination of several axial, shear, and rotational springs, some connected in parallel and others in series, to represent the global response of reinforced concrete. The behavior of each spring is typically modeled using complex, experimentally based hysteretic rules. Some examples of this type of element have been proposed by Kabeyesawa et al. [11] in 1982, Vulcano and Bertero [10] in 1987, Orakcal et al. [3] in 2006, Massone et al. [12] in 2009, Jiang and Kurama [13] in 2010, Panagiotou et al. [14] in 2012, and Kolozvari et al. [15] in 2015.

These macroscopic models are simple and intuitive and have been incorporated into structural nonlinear programs. However, they tend to be problem-based [10], which means they apply only in certain cases.

Microscopic models, on the other hand, are typically based on the finite element method (FEM) and theory of continuum mechanics. In this methodology, a RC wall is divided into a series of elements, over which the respective constitutive law, representing the behavior of the reinforced concrete material, is imposed in a stress–strain space or other possible mixed representation, and the equilibrium equation is satisfied in an average sense with integration over each finite element. The existing microscopic models for reinforced concrete walls can be grouped into three main categories: membrane elements, shell elements and 3D solid brick elements, with the membrane element model being the most commonly used.

The membrane or panel elements display only in-plane behavior (plane stress), typically with two DOFs per node (two displacements). One of the first membrane element formulations used in FEM formulation for the nonlinear analysis of RC walls was that proposed by Cervenka and Gerstle (1970, 1971, 1972) [16]. Cervenka [17] used a quad element with four nodes and two DOFs per node (one horizontal and one vertical displacement), along with a von Mises yield condition, to model concrete. Various researchers have used this type of element or a variation with a larger number of element nodes (i.e., higher elements) but with only two DOFs per node. The main differences between the membrane element formulations proposed over the years have been the constitutive material laws used in the analysis to represent reinforced concrete.

The constitutive laws used to model material behavior are usually nonlinear material models, fracture mechanics models, orthotropic models, plasticity models, hypo-elastic material models, microplane models or nonlocal continuum mechanics models [18,19]. Among the constitutive laws used to represent reinforced concrete in the plane stress condition, the orthotropic models are one of the most widely used types among many researchers [19]. These orthotropic concrete material models are based on the assumption made by Darwin and Pecknold [20] in 1974 and Darwin and Pecknold [21] in 1977. In this assumption, the behavior of a material in biaxial stress can be represented by an equivalent uniaxial strain–stress relation along the principal axis of orthotropy. Orthotropic concrete models have been proposed by Darwin and Pecknold [21], Cervenka [22], Vecchio and Collins [23], Izumo et al. [24], Shin et al. [25], Bolander and Wight [26], Hsu [27], Belarbi and Hsu [28], Pang and Hsu [29], Pang and Hsu [30], Ayoub and Filippou [18], Vecchio [31], Vecchio [32], Palermo and Vecchio [33], Foster and Marti [34], Mansour and Hsu [35], Mansour and Hsu [36], and Zhong [19].

In addition, membrane elements typically use two types of representation to incorporate steel inside RC walls. One type assumes the steel to be a smeared material, which means steel bars are represented as being distributed homogeneously over the element area along the direction of the bars. The second approach uses a truss-type element to represent an actual steel bar. The main drawbacks of this second representation are that the element mesh needs to coincide with the position of the bar in the wall, and elaborate connecting elements between the bar and the membrane element are required to account for bond slippage, if it is considered.

The membrane or panel models generally yield good results compared with experimental data and provide a better and more refined definition of wall structures' local responses. These models tend not to be problem-specific, which allows a variety of problems to be represented with the same procedure. However, the membrane element displacements are typically defined by bilinear interpolation and cannot be easily used in combination with beams because only two displacement degrees of freedom are used at the nodes, and they are more computationally demanding than the macroscopic elements.

This paper develops and presents a formulation of a new quadrilateral layered membrane element with drilling DOFs, which allows for a smoother strain variation over each element and helps the analysis achieve convergence. In addition, this element incorporates one rotational degree of freedom per node, which allows the formulation to be used as a basis for the creation of a shell element to model more complex RC wall structures or to connect the element to beam-type or column-type elements.

The membrane element formulated in this article consists of a quadrilateral element with a total of twelve DOFs, three per node (two displacements and one in-plane rotation) and uses a blended field interpolation for the displacements over the element. The membrane section consists of a layered system of fully bonded, smeared steel reinforcement and smeared orthotropic concrete material with a rotating angle and stiffness tangent formulation, which allows the internal nonlinear behavior of the reinforced concrete wall to be modeled. Additionally, the layered section formulation allows the concrete and steel properties to be changed over the wall thickness and the different wall components, such as the concrete cover, steel rebar and confined concrete, to be properly represented.

The evaluation of the accuracy, applicability, and usefulness of the nonlinear layered quadrilateral membrane in modeling reinforced concrete walls is also presented. A set of experimental results for RC wall elements under monotonic and reversed loads, which are available in the literature, is compared against the results obtained from an analytical model that uses the proposed formulation. These experimental data have previously been used as benchmarks for other models.

2. Quadrilateral layered membrane element with rotational DOF formulation

Membranes are in a state of plane stress, in which only in-plane behavior is considered ($\sigma_z = \tau_{zx} = \tau_{zy} = 0$). The finite element formulation for this type of element, using a displacement-based approach, is well known and can be found in almost any text on

finite elements, such as Bathe [37], Cook et al. [38], and Chen[16]. The formulation is typically developed from the concept of virtual work and is used to determine the plane elements stiffness matrix and resisting force, which are presented next assuming a layered section.

The tangent stiffness of the membrane using a displacement-based approach is defined as

$$K_t = \int_A [B]^T [D_{tangent}][B]dA \tag{1}$$

where

$$[B(x,y)] = \underbrace{\begin{bmatrix} \frac{\partial}{\partial x} & 0 \\ 0 & \frac{\partial}{\partial y} \\ \frac{\partial}{\partial y} & \frac{\partial}{\partial x} \end{bmatrix}}_{[\partial]} [\Psi(x,y)] = [\partial][\Psi(x,y)] \tag{2}$$

and the material tangent matrix $[D_{tangent}]$ that includes the concrete and steel layers over the thickness can be expressed in a discrete manner using the expression applied by Zhang et al. [39] and Zhang et al. [40] in 2007 (Fig. 1) as follows:

$$[D_{Tangent}] = \int_{-\frac{t}{2}}^{\frac{t}{2}} [D]dz = \sum_{i=1}^{Nc} [D_{c_i}](z_{i+1} - z_i) + \sum_{j=1}^{Ns} [D_{s_j}] t_{s_j} \tag{3}$$

where the matrices $[D_{c_i}]$ and $[D_{s_j}]$ are the plane stress material stiffness tangents of the ith concrete layer and jth steel layer, respectively; Nc and Ns are the numbers of layers of concrete and steel, respectively, and z_i is the location of the top and bottom part of each layer; t_{s_j} is the thickness of the section at the jth steel layer.

Similarly, the internal resisting force (R) for the membrane can be defined as follows by integrating over the thickness and assuming zero initial stress:

$$R = \int_A [B]^T \underbrace{\left(\int_{-\frac{t}{2}}^{\frac{t}{2}} \{\sigma\} dz \right)}_{\{\hat{\sigma}\}} dA = \int_A [B]^T \begin{Bmatrix} n_x \\ n_y \\ n_{xy} \end{Bmatrix} dA \tag{4}$$

where the vector stress $\{\hat{\sigma}\}$ can also be calculated in a discrete manner as

$$n_x = \int_{-\frac{t}{2}}^{\frac{t}{2}} \sigma_x dz = \sum_{i=1}^{Nc} \sigma_{x_i}^c (z_{i+1} - z_i) + \sum_{j=1}^{Ns} \sigma_{x_j}^s t_{s_j} \tag{5a}$$

$$n_y = \int_{-\frac{t}{2}}^{\frac{t}{2}} \sigma_y dz = \sum_{i=1}^{Nc} \sigma_{y_i}^c (z_{i+1} - z_i) + \sum_{j=1}^{Ns} \sigma_{y_j}^s t_{s_j} \tag{5b}$$

$$n_{xy} = \int_{-\frac{t}{2}}^{\frac{t}{2}} \tau_{xy} dz = \sum_{i=1}^{Nc} \tau_{xy_i}^c (z_{i+1} - z_i) + \sum_{j=1}^{Ns} \tau_{xy_j}^s t_{s_j} \tag{5c}$$

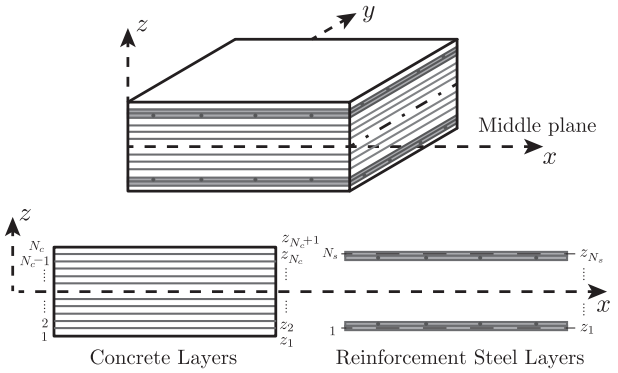

Fig. 1. A typical rectangular layered membrane section.

where $\{\sigma_i^c\}$ represents the in-plane stresses at the ith concrete layer, $\{\sigma_j^s\}$ represents the in-plane stresses at the jth steel layer, and z_{i+1} and z_i are the locations of the top and bottom parts of the ith concrete layer, respectively.

Although the finite element formulation is straightforward, the search for an optimal representation of the displacement field interpolation for the membrane element that includes rotational degrees of freedom remains an area of ongoing research. The next section presents the blended displacement interpolation used in this formulation.

2.1. Blended displacement interpolation

This formulation uses an extension of the field interpolation proposed by Xia et al. [41] in 2009, which allows the interpolations to be used in a general finite element framework with natural coordinates. The blended displacement interpolation proposed in this work is defined as

$$\{u\} = \begin{Bmatrix} u \\ v \end{Bmatrix} = [\Psi(\xi,\eta)]\{U\} \tag{6}$$

with $\{U\}$ representing the displacement at the nodes (see Fig. 2):

$$\{U\} = \{ u_1 \quad v_1 \quad \theta_1 \quad u_2 \quad v_2 \quad \theta_2 \quad u_3 \quad v_3 \quad \theta_3 \quad u_4 \quad v_4 \quad \theta_4 \}^T \tag{7}$$

and $[\Psi(\xi,\eta)]$ is the field interpolation function, defined as follows:

$$[\Psi(\xi,\eta)] = [MN(\xi,\eta)][Tr] \tag{8}$$

where $[Tr]$ is a transformation matrix with the following relationship between the local rotations and the rotations at the nodes:

$$[Tr] = \begin{bmatrix} 1 & 0 & 0 & 0 & 0 & 0 & 0 & 0 & 0 & 0 & 0 & 0 \\ 0 & 1 & 0 & 0 & 0 & 0 & 0 & 0 & 0 & 0 & 0 & 0 \\ 0 & 0 & \frac{y_4-y_1}{2} & 0 & 0 & 0 & 0 & 0 & 0 & 0 & 0 & 0 \\ 0 & 0 & \frac{x_2-x_1}{2} & 0 & 0 & 0 & 0 & 0 & 0 & 0 & 0 & 0 \\ 0 & 0 & 0 & 1 & 0 & 0 & 0 & 0 & 0 & 0 & 0 & 0 \\ 0 & 0 & 0 & 0 & 1 & 0 & 0 & 0 & 0 & 0 & 0 & 0 \\ 0 & 0 & 0 & 0 & 0 & \frac{y_3-y_2}{2} & 0 & 0 & 0 & 0 & 0 & 0 \\ 0 & 0 & 0 & 0 & 0 & \frac{x_2-x_1}{2} & 0 & 0 & 0 & 0 & 0 & 0 \\ 0 & 0 & 0 & 0 & 0 & 0 & 1 & 0 & 0 & 0 & 0 & 0 \\ 0 & 0 & 0 & 0 & 0 & 0 & 0 & 1 & 0 & 0 & 0 & 0 \\ 0 & 0 & 0 & 0 & 0 & 0 & 0 & 0 & \frac{y_3-y_2}{2} & 0 & 0 & 0 \\ 0 & 0 & 0 & 0 & 0 & 0 & 0 & 0 & \frac{x_3-x_4}{2} & 0 & 0 & 0 \\ 0 & 0 & 0 & 0 & 0 & 0 & 0 & 0 & 0 & 1 & 0 & 0 \\ 0 & 0 & 0 & 0 & 0 & 0 & 0 & 0 & 0 & 0 & 1 & 0 \\ 0 & 0 & 0 & 0 & 0 & 0 & 0 & 0 & 0 & 0 & 0 & \frac{y_4-y_1}{2} \\ 0 & 0 & 0 & 0 & 0 & 0 & 0 & 0 & 0 & 0 & 0 & \frac{x_3-x_4}{2} \end{bmatrix} \tag{9}$$

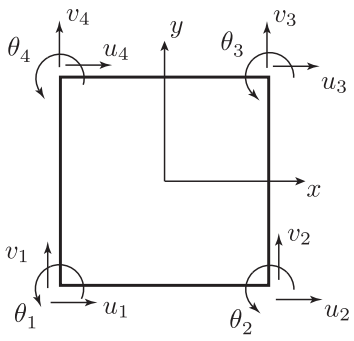

Fig. 2. Element global degrees of freedom used for the blended interpolation.

and $[MN(\xi,\eta)]$ is a matrix containing the shape functions that define the blended interpolation, defined as

$$[MN(\xi,\eta)]=\begin{bmatrix} M_1(\xi)N_1(\eta) & 0 & -M_1(\xi)N_2(\eta) & 0 & M_2(\xi)N_1(\eta) & 0 & -M_2(\xi)N_2(\eta) & 0 & M_2(\xi)N_3(\eta) & 0 & -M_2(\xi)N_4(\eta) & 0 & M_1(\xi)N_3(\eta) & 0 & -M_1(\xi)N_4(\eta) & 0 \\ 0 & M_1(\eta)N_1(\xi) & 0 & M_1(\eta)N_2(\xi) & 0 & M_1(\eta)N_3(\xi) & 0 & M_1(\eta)N_3(\xi) & 0 & M_2(\eta)N_3(\xi) & 0 & M_2(\eta)N_4(\xi) & 0 & M_2(\eta)N_1(\xi) & 0 & M_2(\eta)N_2(\xi) \end{bmatrix} \tag{10}$$

where $M_i(\zeta)$ are the linear shape functions:

$$M_1(\zeta)=\frac{1}{2}(1-\zeta) \qquad M_2(\zeta)=\frac{1}{2}(1+\zeta) \tag{11}$$

and $N_i(\zeta)$ are the Hermitian interpolation functions (cubic interpolations):

$$N_1(\zeta)=\frac{1}{2}-\frac{3}{4}\zeta+\frac{\zeta^3}{4} \tag{12}$$

$$N_2(\zeta)=\frac{1}{4}-\frac{\zeta}{4}-\frac{\zeta^2}{4}+\frac{\zeta^3}{4} \tag{13}$$

$$N_3(\zeta)=\frac{1}{2}+\frac{3}{4}\zeta-\frac{\zeta^3}{4} \tag{14}$$

$$N_4(\zeta)=-\frac{1}{4}-\frac{\zeta}{4}+\frac{\zeta^2}{4}+\frac{\zeta^3}{4} \tag{15}$$

Now, it is possible to define the kinematic matrix $[B]$ in Eq. (2) as follows:

$$[B]=[A]\begin{bmatrix}[J]^{-1} & [0]\\ [0] & [J]^{-1}\end{bmatrix}\begin{bmatrix}\frac{\partial MN_{1,i}}{\partial\xi}\\ \frac{\partial MN_{1,i}}{\partial\eta}\\ \frac{\partial MN_{2,i}}{\partial\xi}\\ \frac{\partial MN_{2,i}}{\partial\eta}\end{bmatrix}[Tr] \tag{16}$$

where $[A]$ is the matrix defined in Eq. (17)

$$[A]=\begin{bmatrix}1 & 0 & 0 & 0\\ 0 & 0 & 0 & 1\\ 0 & 1 & 1 & 0\end{bmatrix} \tag{17}$$

and $[J]^{-1}$ is the inverse of the Jacobian matrix ($[J]$), which relates the natural coordinate system and local coordinate system of each element. The Jacobian matrix and the inverse of the Jacobian matrix are defined as follows:

$$\begin{Bmatrix}\frac{\partial}{\partial\xi}\\ \frac{\partial}{\partial\eta}\end{Bmatrix}=\underbrace{\begin{bmatrix}\frac{\partial X(\xi,\eta)}{\partial\xi} & \frac{\partial Y(\xi,\eta)}{\partial\xi}\\ \frac{\partial X(\xi,\eta)}{\partial\eta} & \frac{\partial Y(\xi,\eta)}{\partial\eta}\end{bmatrix}}_{[J]}\begin{Bmatrix}\frac{\partial}{\partial x}\\ \frac{\partial}{\partial y}\end{Bmatrix} \tag{18}$$

and

$$\begin{Bmatrix}\frac{\partial}{\partial x}\\ \frac{\partial}{\partial y}\end{Bmatrix}=\underbrace{\frac{1}{|J|}\begin{bmatrix}\frac{\partial Y(\xi,\eta)}{\partial\eta} & \frac{-\partial Y(\xi,\eta)}{\partial\xi}\\ \frac{-\partial X(\xi,\eta)}{\partial\eta} & \frac{\partial X(\xi,\eta)}{\partial\xi}\end{bmatrix}}_{[J]^{-1}}\begin{Bmatrix}\frac{\partial}{\partial\xi}\\ \frac{\partial}{\partial\eta}\end{Bmatrix} \tag{19}$$

where X and Y represent the geometry of the element using natural coordinates:

$$X(\xi,\eta)=\sum_{i=1}^{4}\psi_i(\xi,\eta)x_i \tag{20}$$

$$Y(\xi,\eta)=\sum_{i=1}^{4}\psi_i(\xi,\eta)y_i \tag{21}$$

x_i and y_i are the coordinates of the corner nodes and $\psi_i(\xi,\eta)$ are the bilinear shape functions, which are defined as follows:

$$\psi_i(\xi,\eta)=\frac{1}{4}(1+\xi_i\xi)(1+\eta_i\eta) \qquad i=1,2,3,4 \tag{22}$$

where $\xi_i=[-1 \;\; 1 \;\; 1 \;\; -1]$ and $\eta_i=[-1 \;\; -1 \;\; 1 \;\; 1]$ for $i=1,2,3,4$ are the coordinates of the nodes in the natural coordinate system.

The next section presents the material constitutive model used in each layer to represent the concrete in two directions and the steel rebar inside the RC.

3. Material constitutive models

This section presents the material constitutive laws used to define the concrete and the steel rebar inside the RC walls. It was concluded that a separate constitutive model representing the concrete as smeared concrete layers and the steel rebar as smeared steel layers was necessary to implement a layered section approach [42].

3.1. Formulation of the concrete constitutive model

Of the constitutive material laws available for the modeling of concrete in two directions, the smeared cracked concrete models, which are based on the assumption that different cracks over an area can be modeled using the concrete average stress–strain relation in that zone, are the preferred models. Among the smeared cracked models, an orthotropic model, with equivalent uniaxial average stress–strain relations along the axes of orthotropy, was selected because orthotropic models are noted for their simplicity and are sufficiently robust to represent concrete material behavior, showing excellent agreement with the experimental data as mentioned by Ayoub and Filippou [18] in 1998. The axes of orthotropy were assumed to coincide with the principal axes of total strain, and the model was developed using a tangent stiffness-based approach for use in a general nonlinear finite element program.

In addition, this concrete model incorporated characteristics from the models created by a research group from the University of Houston, such as the CSMM presented by Zhong [19] in 2005, and the models created by a research group from the University of Toronto, including the expanded MCFT developed by Palermo [43] in 2002 and Palermo and Vecchio [33] in 2003 and the concrete model created by Vecchio [44] in 1992. Other additional characteristics were incorporated to consider the effect of biaxial compression or tension–compression (softening) along the axes of orthotropy, as well as to account for damage in the material during cycling loads and enhancement due to confinement. The different features in the model were employed for the procurement of a numerically stable, reliable and efficient constitutive material.

The behavior of the concrete along the directions of principal stress is defined by average uniaxial stress–strain relations. In this study, these relations were represented by uniaxial concrete material models. The variables of each average uniaxial relations are tracked along the rotating directions inside of each possible quadrant of rotation, which are defined as $-\pi/4$ to $\pi/4$ and $\pi/4$ to $3\pi/4$. Using this simplification, each average uniaxial relation represents the behavior of the material contained within one quadrant. Among the different uniaxial concrete materials available in the literature, it was determined that the model proposed by Massone et al. [12] in 2009 for static loading, and extended here to include hysteretic rules, is the one that best represented the average uniaxial stress–strain relations for the principal stress directions in the smeared rotating angle concrete model in this study.

The basic assumptions used to formulate the concrete material were as follows:

- The principal strain and stress directions coincide.
- The stress–strain relation can be represented by the average stress–strain.
- The constitutive model for concrete in each of the principal stress directions can be represented by a uniaxial concrete model.
- The Poisson ratio is neglected after cracking.

The last assumption was used to improve the convergence of the model because if the Poisson ratio is maintained, the material tangent matrix is not symmetric and can cause some instability in the model after cracking of the material, and it was observed that the contribution after cracking in the results was not significant. Using these assumptions, the transformation of the strain and stress between coordinate systems and the derivation of the principal strain direction, the biaxial strain (ε_{11} and ε_{22}) in the principal directions of strain can be determined as follows:

$$\varepsilon_{11} = \frac{1}{2}(\varepsilon_{xx} + \varepsilon_{yy}) + \frac{1}{2}\sqrt{(\varepsilon_{xx} - \varepsilon_{yy})^2 + (\gamma_{xy})^2} \tag{23a}$$

$$\varepsilon_{22} = \frac{1}{2}(\varepsilon_{xx} + \varepsilon_{yy}) - \frac{1}{2}\sqrt{(\varepsilon_{xx} - \varepsilon_{yy})^2 + (\gamma_{xy})^2} \tag{23b}$$

where ($\{\varepsilon_{x-y}\} = \{\varepsilon_{xx} \quad \varepsilon_{yy} \quad \gamma_{xy}\}^T$) are the strain components in the local coordinate system ($x-y$) of the concrete layer. These components can be represented in matrix form as

$$\begin{Bmatrix} \varepsilon_{11} \\ \varepsilon_{22} \\ \gamma_{12} \end{Bmatrix} = [T_{strain}(\theta_{pd})] \begin{Bmatrix} \varepsilon_{xx} \\ \varepsilon_{yy} \\ \gamma_{xy} \end{Bmatrix} \tag{24}$$

where $[T_{strain}(\theta)]$ is the strain transformation matrix, defined as follows:

$$[T_{strain}(\theta)] = \begin{bmatrix} \cos^2(\theta) & \sin^2(\theta) & \sin(\theta)\cos(\theta) \\ \sin^2(\theta) & \cos^2(\theta) & -\sin(\theta)\cos(\theta) \\ -2\sin(\theta)\cos(\theta) & 2\sin(\theta)\cos(\theta) & \cos^2(\theta) - \sin^2(\theta) \end{bmatrix} \tag{25}$$

and θ_{pd} is the angle of the principal strain direction of strain (see Fig. 3), defined by

$$\theta_{pd} = \frac{1}{2} arctan\left(\frac{\gamma_{xy}}{(\varepsilon_{xx} - \varepsilon_{yy})}\right) \tag{26}$$

Recall that for principal strain, $\gamma_{12} = 0$.

Now, the biaxial strains must be transformed into uniaxial strains so that this result can be used in the uniaxial stress–strain relation for each axis of orthotropy. The Poisson ratio (ν_{12}, ν_{21}) is used here. This transformation has been studied and discussed extensively by the research groups from the University of Houston and the University of Toronto. This formulation uses the transformation presented in Zhong [19] in 2005 but with the Poisson ratio proposed by Vecchio [44] in 1992. This relation between the biaxial strain and uniaxial strain results in the following set of equations:

$$\bar{\varepsilon}_1 = \frac{1}{1 - \nu_{12}\nu_{21}}\varepsilon_1 + \frac{\nu_{12}}{1 - \nu_{12}\nu_{21}}\varepsilon_2 \tag{27a}$$

$$\bar{\varepsilon}_2 = \frac{\nu_{21}}{1 - \nu_{12}\nu_{21}}\varepsilon_1 + \frac{1}{1 - \nu_{12}\nu_{21}}\varepsilon_2 \tag{27b}$$

The equations can also be written in matrix form:

$$\begin{Bmatrix} \bar{\varepsilon}_{11} \\ \bar{\varepsilon}_{22} \\ \bar{\gamma}_{12} \end{Bmatrix} = [V] \begin{Bmatrix} \varepsilon_{11} \\ \varepsilon_{22} \\ \gamma_{12} \end{Bmatrix} \tag{28}$$

where

$$[V] = \begin{bmatrix} \frac{1}{1-\nu_{12}\nu_{21}} & \frac{\nu_{12}}{1-\nu_{12}\nu_{21}} & 0 \\ \frac{\nu_{21}}{1-\nu_{12}\nu_{21}} & \frac{1}{1-\nu_{12}\nu_{21}} & 0 \\ 0 & 0 & 1 \end{bmatrix} \tag{29}$$

and

$$\nu_{ij} = \begin{cases} 0.2 & \text{if} \quad \varepsilon_j > \frac{\varepsilon_{c_0}}{2} \\ 0.2\left(1 + 1.5\left(\frac{2\varepsilon_j}{\varepsilon_{c_0}} - 1\right)^2\right) \not> 0.5 & \text{if} \quad \frac{\varepsilon_{c_0}}{2} \geqslant \varepsilon_j \end{cases} \tag{30}$$

To obtain a stable solution, the values of the Poisson ratio (ν_{12}, ν_{21}) after cracking are neglected (considered equal to zero).

Using the uniaxial strain $\bar{\varepsilon}_{11}$ and $\bar{\varepsilon}_{22}$, and recalling that $\bar{\gamma}_{12} = \gamma_{12} = 0$, the concrete stress in the direction of orthotropy or the principal stress direction can be defined as a function of this uniaxial strain as $\sigma_{11}(\bar{\varepsilon}_{11}, \bar{\varepsilon}_{22})$ and $\sigma_{22}(\bar{\varepsilon}_{11}, \bar{\varepsilon}_{22})$. Because of the assumption that the principal stress and strain directions coincide, it is possible to determine the stress in the local coordinates $x-y$ using the transformation defined by the angle θ_{pd} as follows:

$$\begin{Bmatrix} \sigma^c_{xx} \\ \sigma^c_{yy} \\ \tau^c_{xy} \end{Bmatrix} = [T_{stress}(-\theta_{pd})] \begin{Bmatrix} \sigma^c_{11} \\ \sigma^c_{22} \\ 0 \end{Bmatrix} = [T_{strain}(\theta_{pd})]^T \begin{Bmatrix} \sigma^c_{11} \\ \sigma^c_{22} \\ 0 \end{Bmatrix} \tag{31}$$

where the stress transformation matrix is defined as follows:

$$[T_{stress}(\theta)] = \begin{bmatrix} \cos^2(\theta) & \sin^2(\theta) & 2\sin(\theta)\cos(\theta) \\ \sin^2(\theta) & \cos^2(\theta) & -2\sin(\theta)\cos(\theta) \\ -\sin(\theta)\cos(\theta) & \sin(\theta)\cos(\theta) & \cos^2(\theta) - \sin^2(\theta) \end{bmatrix} \tag{32}$$

Now, using the definitions for strain and stress presented above, the tangent material constitutive matrix for the concrete layer in the local coordinate system ($x-y$) can be defined as

$$\left[D^c_{x-y}\right] = \frac{\partial \sigma_{x-y}}{\partial \varepsilon_{x-y}} = \frac{\partial \begin{Bmatrix} \sigma_{xx} \\ \sigma_{yy} \\ \tau_{xy} \end{Bmatrix}}{\partial \begin{Bmatrix} \varepsilon_{xx} \\ \varepsilon_{yy} \\ \gamma_{xy} \end{Bmatrix}} = [T_{strain}(\theta_{pd})]^T [D^c_{1-2}][V][T_{strain}(\theta_{pd})] \tag{33}$$

where $[D^c_{1-2}]$ is the material tangent matrix for the concrete layer in the principal strain (or stress) direction and can be defined as proposed by Crisfield and Wills [45] in 1989:

$$[D^c_{1-2}] = \begin{bmatrix} \frac{\partial \sigma_{11}}{\partial \varepsilon_{11}} & \frac{\partial \sigma_{11}}{\partial \varepsilon_{22}} & 0 \\ \frac{\partial \sigma_{22}}{\partial \varepsilon_{11}} & \frac{\partial \sigma_{22}}{\partial \varepsilon_{22}} & 0 \\ 0 & 0 & \frac{\sigma_{11} - \sigma_{22}}{2(\varepsilon_{11} - \varepsilon_{22})} \end{bmatrix} \tag{34}$$

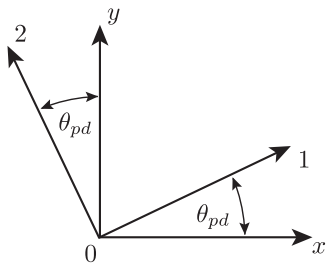

Fig. 3. Principal strain direction.

For simplicity and stability, $\frac{\partial \sigma_{11}}{\partial \varepsilon_{22}}$ and $\frac{\partial \sigma_{22}}{\partial \varepsilon_{11}}$ are neglected, which reduces Eq. (34) to

$$\left[D^c_{1-2}\right] = \begin{bmatrix} \frac{\partial \sigma_{11}}{\partial \varepsilon_{11}} & 0 & 0 \\ 0 & \frac{\partial \sigma_{22}}{\partial \varepsilon_{22}} & 0 \\ 0 & 0 & \frac{\sigma_{11}-\sigma_{22}}{2(\varepsilon_{11}-\varepsilon_{22})} \end{bmatrix} \tag{35}$$

The uniaxial concrete material used in this formulation is now reviewed.

3.1.1. Uniaxial concrete models using the Thorenfeldt curve

This uniaxial concrete model was proposed by Massone et al. [12] in 2009 for static loading, and it is extended here to include hysteretic rules. This section presents the main characteristics, rules and equations that define the model proposed by Massone et al. [12] and extended to include hysteretic rules. The model envelope is composed of two different equations: one is used for the compression envelope (see Fig. 4), and the other is for the tension envelope (see Fig. 5).

The compression envelope is defined by the curve proposed by Thorenfeldt et al. [46] in 1987, which is similar to the equation defined by Popovics [47] in 1973. The Thorenfeldt base curve was later calibrated by Collins and Porasz [48] in 1989 (see Fig. 4) and was used for shells and membranes by Polak and Vecchio [49] in 1993 and Vecchio and Collins [50] in 1993; it was then used in MVLM by Orakcal et al. [3] and Massone et al. [12] in 2009. The curve can be defined as

$$\sigma_c(\varepsilon_c) = f'_c \frac{n\left(\frac{\varepsilon_c}{\varepsilon_{c_0}}\right)}{n-1+\left(\frac{\varepsilon_c}{\varepsilon_{c_0}}\right)^{nk}} \tag{36}$$

where f'_c is the peak resistant stress of the concrete in compression, ε_{c_0} is the strain at the peak resistant stress of the concrete in compression, and n and k are the parameters calibrated by Collins and Porasz [48] in 1989, as follows:

$$n = 0.8 + \frac{f'_c(\text{MPa})}{17} = 0.8 + 0.41 f'_c(\text{ksi}) \tag{37a}$$

$$k = \begin{cases} 1 & \text{if} \quad 0 \leqslant \varepsilon_c \leqslant \varepsilon_{c_0} \\ 0.67 + \frac{f'_c(\text{MPa})}{62} = 0.67 + \frac{f'_c(\text{ksi})}{9} & \text{if} \quad \varepsilon_c > \varepsilon_{c_0} \end{cases} \tag{37b}$$

Carreira and Kuang-Han [51] proposed parameter calibration for concrete with a lower compressive resistant stress as follows:

$$n = 1.55 + \left(\frac{f'_c(\text{MPa})}{32.4}\right)^3 = 1.55 + \left(\frac{f'_c(\text{ksi})}{4.7}\right)^3 (\text{ksi}) \tag{38a}$$

$$k = 1 \tag{38b}$$

The tension envelope used by Massone et al. [12] is that proposed by Belarbi and Hsu [52] in 1994, which is based on the equation used by Tamai et al. [53] in 1988. Belarbi and Hsu [52] proposed this model after testing 17 reinforced concrete panels under pure tension. The tension envelope is divided into two sections (see Fig. 5), pre-peak or pre-cracking and post-peak or post-cracking. A linear interpolation is selected before cracking, and a descending branch is selected for post-cracking to include the tension stiffening observed in the average stress–strain relation of the concrete in tension (Eq. (39)).

$$\sigma_c(\varepsilon_c) = \begin{cases} \left(\frac{f_{cr}}{\varepsilon_{cr}}\right)\varepsilon_c & \text{if} \quad \varepsilon_c \leqslant \varepsilon_{cr} \\ f_{cr}\left(\frac{\varepsilon_{cr}}{\varepsilon_c}\right)^b & \text{if} \quad \varepsilon_c > \varepsilon_{cr} \end{cases} \tag{39}$$

where b is a parameter that defines the descending branch of the envelope in tension, f_{cr} is the peak of the concrete resistant stress in tension, and ε_{cr} is the strain at the peak of the concrete resistant stress in tension. Belarbi and Hsu [52] proposed the value $b = 0.4$ and the following values for the other parameters:

$$f_{cr} = 0.31\sqrt{f'_c(\text{MPa})}[\text{MPa}] \quad \text{or} \quad f_{cr} = 0.118\sqrt{f'_c(\text{ksi})}[\text{ksi}] \tag{40a}$$

$$\varepsilon_{cr} = 0.00008 \tag{40b}$$

For the cyclic loading behavior of concrete, a hysteric rule that use a series of straight lines, similar to the rule proposed by Mohd Yassin [54] in 1994, is used. However, in this work, an origin-oriented approach was not used; instead, the expression in Eq. (41) for compression was selected to determine the concrete plastic strain (ε^c_p) at each full unloading, which is the unrecovered strain deformation in the material. The representation for unloading and reloading in compression is created by graphing a linear equation with a slope equal to the initial stiffness of the concrete (E_{c_0}) until this line intercepts the linear equation for the unloading path with a slope in the compression zone equal to $0.071E_{c_0}$, which is the same value proposed by Palermo and Vecchio [33] in 2003 and the origin in the concrete plastic strain, or the intercept of the reloading path in compression, which is a line that connects the plastic strain and the last point in the envelope equation in compression (see Fig. 6).

$$\varepsilon^c_p = \varepsilon^c_m\left(1 - e^{-\left(\frac{\varepsilon^c_m}{\varepsilon_{c_0}}\right)\alpha_c}\right) \tag{41}$$

where ε^c_m is the maximum previous compressive strain recorded in the material and α_c is a parameter that determines the amount of plastic strain in the concrete. A value of $\alpha_c = 0.32$ was used for the analysis in this study.

Linear paths with a slope equal to the previous unloading stiffness of the concrete in tension were selected for the unloading and reloading rules in tension (see Fig. 6), and the slopes for this part were defined using a plastic strain determinate as follows:

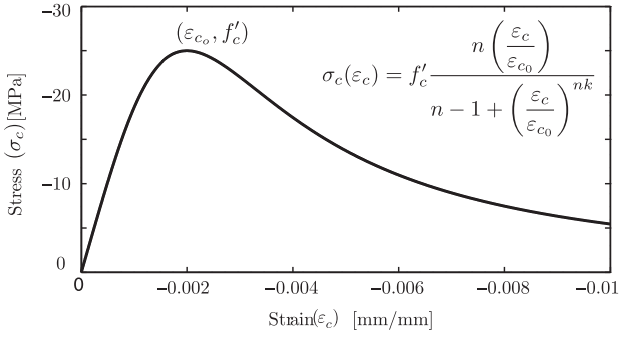

Fig. 4. Constitutive model for concrete in compression using the Thorenfeldt curve.

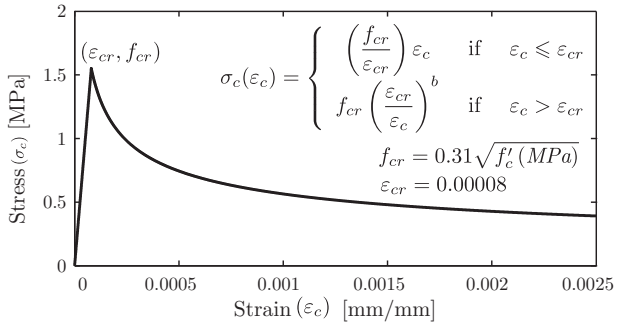

Fig. 5. Constitutive model for concrete in tension using the Belarbi and Hsu [52] equation.

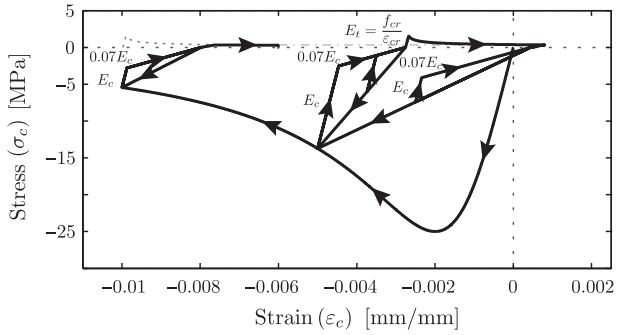

Fig. 6. Hysteretic rules for the concrete model.

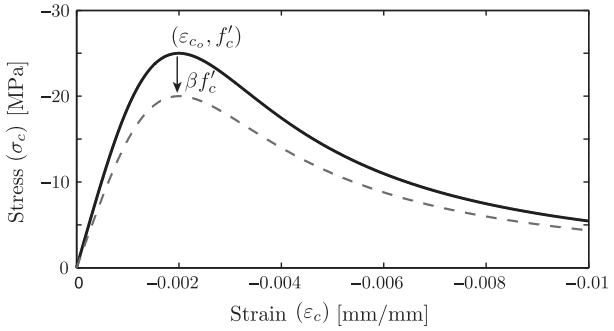

Fig. 7. Compression softening effect.

$$\varepsilon_p^t = \varepsilon_m^t \left(1 - e^{-\left(\frac{\varepsilon_m^t}{\varepsilon_{cr}}\right)\alpha_t}\right) \tag{42}$$

where ε_{im}^c is the maximum previous tension strain recorded in the material and α_t is a parameter that determines the amount of plastic strain in the concrete. A value of $\alpha_t = 0.08$ was used in this study. A shift in the tension envelope's origin (see Fig. 6) was considered to produce a more accurate model, reduce pinching, and to be able to model the gap closure with a linear path.

3.1.2. Modification coefficients for the concrete model

This section presents the functions of the coefficients used to account for compression softening, the enhancement due to biaxial compression, and the damage due to cyclic or reversal loading in a concrete material in a biaxial stress state. Such behavior has been extensively observed and discussed in the literature (e.g., [23,28,18,55,56,33,19,12]). Various equations have been developed to account for this behavior. These coefficients typically modify the peak resistant stress of the concrete in compression (f'_c) and sometimes the strain at the peak resistant stress of the concrete in compression (ε_{c_0}). However, only a modification to f'_c was applied in the analysis conducted in this study, as suggested by Massone et al. [12], because Vecchio and Collins [50] observed that more sophisticated models result in only marginally better solutions [12]. Moreover, only f'_c was modified to maintain a stable and efficient numerical solution.

The compression softening effect ($\beta_s f'_c$) is the reduction in the concrete compression resistance along one direction due to tension strain in the perpendicular direction (see Fig. 7). This effect was modeled using the coefficient proposed by Belarbi and Hsu [28] in 1995 and was defined as

$$\beta_s = \frac{k}{\sqrt{1 + k_\sigma \varepsilon_{tension}}} \tag{43}$$

where $\varepsilon_{tension}$ is the tension strain in concrete and k and k_σ are two parameters that define the reduction factor. The factor k_σ was defined as 250 for sequential loading and 400 for proportional loading [28], and k was defined as 0.9 by Belarbi and Hsu [28]. However, it was observed that a value of 1 for k resulted in more stable solutions without much loss of accuracy.

Compression strength enhancement ($\beta_e f'_c$) is an increase in the concrete peak resistant stress f'_c and can be produced by the biaxial compression stress state, as indicated by Kupfer et al. [57] in 1969 and Vecchio [44] in 1992, or by the confinement produced by stirrups, cross ties and hoops in concrete, as explored by Mander et al. [58] in 1988. The enhanced compression strength due to biaxial compression is considered using the equation (Eq. (44)) proposed by Vecchio [44] in 1992:

$$\beta_{e_{ij}} = 1 + 0.92\left(\frac{\sigma_{c_j}}{f'_c}\right) - 0.76\left(\frac{\sigma_{c_j}}{f'_c}\right)^2 \tag{44}$$

where i is the direction being enhanced, j is the direction normal to i, σ_{c_j} is the stress in the direction normal to i, and f'_c is the peak resistant stress of the concrete in compression.

Damage due to cyclic or reversal loading ($\beta_d f'_c$) is defined as the deterioration of concrete compression strength under cyclic loading and unloading. This effect was studied by Palermo and Vecchio [33] in 2003, who proposed an equation for deterioration in compression and tension that is a function of the difference between the maximum and minimum strain occurring during reverse loading. Only the damage in compression was used in this study. The equation proposed by Palermo and Vecchio [33] can be written as

$$\beta_d = \frac{1}{1 + \alpha_1 \left(\frac{\varepsilon_{rec}}{\varepsilon_{c_0}}\right)^{\alpha_2}} \tag{45}$$

where ε_{c_0} is the strain at the peak resistant stress of the concrete in compression, the parameter α_1 is equal to 0.5 for pre-cracking and 0.6 for post-cracking in compression, α_2 is equal to 0.1 for pre-cracking and 0.175 for post-cracking in compression, and ε_{rec} is defined as

$$\varepsilon_{rec} = \varepsilon_{max} - \varepsilon_{min} \tag{46}$$

where ε_{max} is the maximum strain recorded during cyclic loading and ε_{min} is the minimum strain.

An additional factor was used to account for the enhancement due to confinement (β_{conf}). This factor was applied over the compression peak strength of the concrete (f'_c) as $\beta_{conf} f'_c$ at the beginning of the analysis and maintained constant during the remainder of the analysis. The factor can be created using the sophisticated equation proposed by Mander et al. [58] in 1988 or a more simple coefficient such as that used by Orakcal et al. [3] in 2006 and defined as

$$\beta_{conf} = 1 + \frac{\rho_s f_y}{f'_c} \tag{47}$$

where ρ_s is the ratio between the volume of transverse steel and the volume of core concrete measured from the outside of the stirrups, f_y is the yield strength of the transverse steel, and f'_c is the peak resistant stress of the concrete in compression.

3.2. Formulation of the constitutive model for steel

In this formulation, the steel bars were considered to be a layer of homogeneous material inside the concrete element, and the variation stress due to cracking over an area was modeled using the average stress–strain of the steel in that zone. In addition, it was assumed that the smeared steel worked only in the direction of the bars because these bars were typically in a uniaxial state of stress. This assumption allowed for the use of a uniaxial constitutive model to represent the reinforcing steel bars. Two uniaxial

steel material models were used in this formulation, the well-known Menegotto–Pinto steel model proposed by Menegotto and Pinto [59] in 1973 and the model proposed by Massone and Moroder [60] in 2009.

The smeared steel material used in this study assumes the following:

- Steel is considered smeared and acts only along the direction of its orientation.
- The stress–strain relation can be represented by the average stress–strain relation of steel bars embedded in the concrete.
- Concrete and smeared steel are considered fully bonded.
- The Poisson ratio is neglected after cracking.

Using these assumptions, and an approach similar to that proposed by Zhong [19] in 2005, the uniaxial strain in the steel orientation can be written as

$$\{\varepsilon_s\} = [T_{strain}(\theta_s - \theta_{pd})][V][T_{strain}(\theta_{pd})] \begin{Bmatrix} \varepsilon_{xx} \\ \varepsilon_{yy} \\ \varepsilon_{xy} \end{Bmatrix} \tag{48}$$

where $[T_{strain}(\theta)]$ is the strain transformation defined by Eq. (25), θ_s is the angle that defines the orientation of the steel layer with respect to the local coordinate system $(x-y)$ (see Fig. 8), θ_{pd} is the orientation of the principal strain direction defined by Eq. (26), and $[V]$is the Poisson ratio matrix of the strain vector defined by Eq. (30). Because the steel is considered a uniaxial material, the only component needed is the strain in the steel direction, which is represented by the component ε_{s_1}. This strain is used to determine the stress $(f_s(\varepsilon_{s_1}))$ and the stiffness tangent $\left(E_s(\varepsilon_{s_1}) = \frac{\partial f_s}{\partial \varepsilon_s}\right)$ in the direction of the smeared steel action from the average uniaxial stress–strain relations, which are presented in the next section. Using these values, the stiffness tangent of the layer in the plane stress state for the coordinate system $(x-y)$ can be determined as follows:

$$\left[D^s_{x-y}\right] = [T_{strain}(\theta_s)]^T [D_s][T_{strain}(\theta_s - \theta_{pd})][V][T_{strain}(\theta_{pd})] \tag{49}$$

or for simplicity, without considering the Poisson ratio, as follows:

$$\left[D^s_{x-y}\right] = [T_{strain}(\theta_s)]^T [D_s][T_{strain}(\theta_s)] \tag{50}$$

where

$$[D_s] = \begin{bmatrix} \rho E^s_t & 0 & 0 \\ 0 & 0 & 0 \\ 0 & 0 & 0 \end{bmatrix} \tag{51}$$

and ρ is the ratio of reinforced steel in the layer and E^s_t is the tangential stiffness of the smeared steel.

Furthermore, the resistant stress of the smeared steel layer in the coordinate system $(x-y)$ can be determined as

$$\begin{Bmatrix} \sigma^s_{xx} \\ \sigma^s_{yy} \\ \tau^s_{xy} \end{Bmatrix} = [T_{stress}(-\theta_s)] \begin{Bmatrix} \rho f_s \\ 0 \\ 0 \end{Bmatrix} = [T_{strain}(\theta_s)]^T \begin{Bmatrix} \rho f_s \\ 0 \\ 0 \end{Bmatrix} \tag{52}$$

with the stress transformation matrix defined by Eq. (25).

As previously mentioned, the action of the smeared steel in its orientation was modeled using average uniaxial stress–strain relations. Different steel materials have been implemented to determine the uniaxial stress–strain relation of steel bars inside concrete. It is commonly assumed in models that the behavior of steel bars with and without concrete is identical. However, Tamai et al. [53], who obtained a set of experimental data for reinforced concrete prisms, observed that the behavior of reinforcing steel inside concrete presents some differences from that of bare steel.

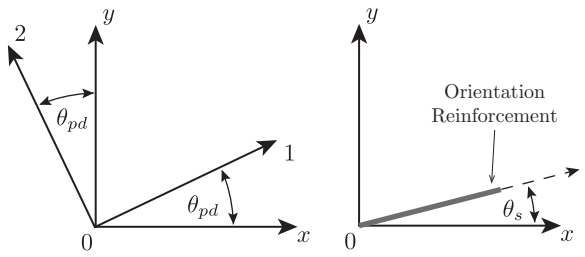

Fig. 8. Steel layer orientation.

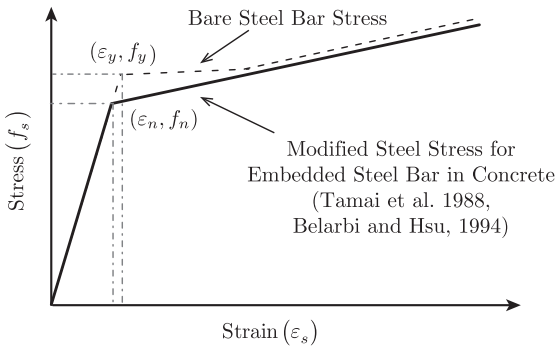

Fig. 9. Stress–strain relation of embedded steel bars in concrete and bare steel bars.

This effect was corroborated by Belarbi and Hsu [28] in 1995. Fig. 9 shows the behavior observed for reinforcing steel bars embedded in the concrete. This behavior can be modeled as a reduction in the yield strength and strain-hardening ratio compared with that of bare steel bars. This variation in the behavior of steel was attributed to the consideration of the steel stress as a function of the average concrete strain, meaning that although the steel could already have started to yield in the crack, the steel stress will be smaller in between cracks [52].

Due to the effect observed and studied by Belarbi and Hsu [28] in 1995, the average uniaxial stress–strain relations used are modeled by uniaxial steel material models with a reduction in the position of the yield strength (f_y) and strain-hardening ratio (b). In the following sections, the uniaxial steel models used in this work are reviewed.

3.2.1. Uniaxial Menegotto–Pinto steel model

This model corresponds to the well-known Menegotto–Pinto model of 1973 [59], which was modified by Filippou et al. [61] in 1983 to include isotropic hardening by shifting the yield stress asymptote. This model is computationally efficient and can accurately represent the Bauschinger effects and the behavior of experimentally observed reinforcing steel bars [3]. See Fig. 10. The value of the parameters for this model used in this study are $R_0 = 18, a_1 = 16.2$, and $a_2 = 0.15$.

To use this uniaxial model for average stress–strain relationships, the values of $f_y^{average}$ and $b_{average}$ need to be modified to account for the behavior of the stress–strain relationships for steel bars embedded in concrete, as shown by Belarbi and Hsu [52] in 1994:

$$f_y^{average} = (0.91 - 2B) f_y \tag{53a}$$

$$b_{average} = (0.02 + 0.25B) b \tag{53b}$$

3.2.2. Uniaxial Massone-Moroder steel model

The second model used in this work is that proposed by Massone and Moroder [60] in 2009, which is capable of representing buckling of longitudinal reinforcing bars. This model is based

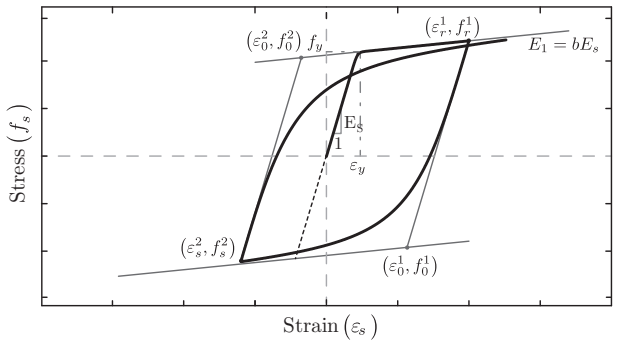

Fig. 10. Constitutive Menegotto–Pinto model for steel.

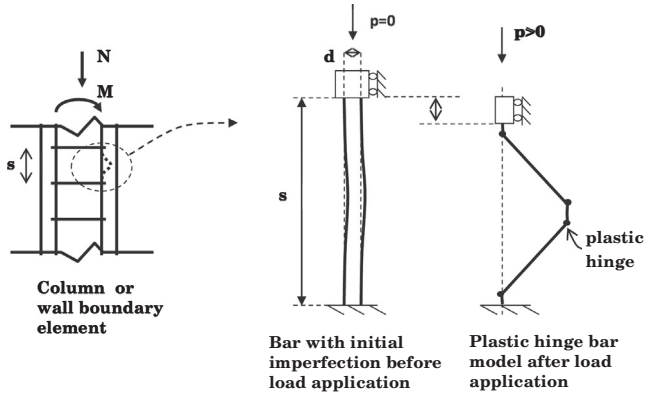

Fig. 11. Bar buckling model (after [60]).

on a concentrated plasticity fiber model that considers four plastic hinges located at the zones of maximum moment (Fig. 11), which occurs during the introduction of an imperfection and deformation due to the axial load applied in the reinforcing bar. Sectional analysis, based on uniaxial constitutive material laws for steel, is used, and moment equilibrium is imposed in the section, resulting in a nonlinear equation (geometric and material nonlinearity) that requires an iterative procedure on the section curvature. Moreover, the cyclic model is based on a simple phenomenological formulation that incorporates the Bauschinger effect in the unloading and reloading rules. This uniaxial steel model was only used in the analysis of the test experiment performed by Yañez [62] in 1993, in which the steel model was calibrated to match the experimental data (yield stress and ultimate stress).

4. Verification

The RC wall tests used in this study were selected after a thorough revision of the available experimental results in the literature. The experimental data can be divided into monotonic loading and reversed or cyclic loading. For monotonic loading, this study used the experimental result of the tests of a wall presented by Cervenka [17] in 1971 and the experiment results of the tests of two types of walls presented by Lefas et al. [63] in 1990. For reversal or cyclic loading, this study used the experimental results of the tests of two rectangular single walls reported by Thomsen and Wallace [64] in 1995 and the experiment result of a reinforced concrete wall with irregulars disposition of openings reported by Yañez [62] in 1993.

In all the models presented next, the tensile strength of the concrete (f_{cr}) was considered equal to $0.31\sqrt{f'_c\ [\text{MPa}]}$ ($0.118\sqrt{f'_c\ [\text{ksi}]}$), and the tension strain ε_{cr} at the maximum tensile strength was equal to 0.00008 [mm/mm]; moreover, a compression strain between −0.003 and −0.0055 [mm/mm] at the maximum compressive strength of concrete for the different specimens in the confined concrete, depending on the level of confinement, was used. In addition, for steel, a base value of 1% for the hardening ratio (b in Eq. (53b)) and a value of $Es = 200,000$ [MPa] for the Young's modulus of the steel were used when no experimental value was available to calibrate. Moreover, a 3-by-3 Gauss integration in each element for the analysis of the panel and the abovementioned element were used. The analytical models were analyzed using the displacement control solution algorithm with pseudo-constant incremental steps, which indicate that if the analysis has not reached convergence for an increment of displacement, the increment is reduced until the initial increment has passed; this is a variation of the algorithm developed by Batoz and Dhatt [65] in 1979.

4.1. Monotonic loading

The following section evaluates and verifies the nonlinear layered quadrilateral membrane elements with drilling degrees of freedom using experimental test walls under monotonic loads available in the literature.

4.1.1. Reinforced concrete wall – Cervenka and Gerstle

Cervenka [17] in 1970 presented the results for a series of tests using reinforced concrete panels. These panels were built and loaded in groups of two, which were bounded by thickened ribs on each side of the panel, forming a deep beam (see Fig. 12). The loading was performed at the middle of the deep-beam specimen (center rib), which was simply supported at the end, as shown in Fig. 12. The specimens measured 760 [mm] (30 [in]) in height, 760 [mm] (30 [in]) in width, and 51 [mm] (2 [in]) or 75 [mm] (3 [in]) in thickness, with thickened ribs measuring 300 [mm] (11.75 [in]) by 102 [mm] (4 [in]), and were reinforced with orthogonal reinforcement (horizontal and vertical) at the center of the section of each panel (Fig. 12).

To validate the proposed analytical model, the reinforced concrete specimen W2 was selected (Fig. 12), which has been used as a benchmark by other authors [20,66,18]. This test was selected because the specimen has various ratios of horizontal steel over the model height and a constant ratio of steel in the vertical direction (Fig. 12), which makes the model an interesting case study.

For the horizontal and vertical reinforcement bars, No 3 were used with a cross-sectional area of 70 [mm^2] (0.11 [in^2]), a yielding strength of $f_y = 353$ [MPa], (51.2 [ksi]) and a Young's modulus of

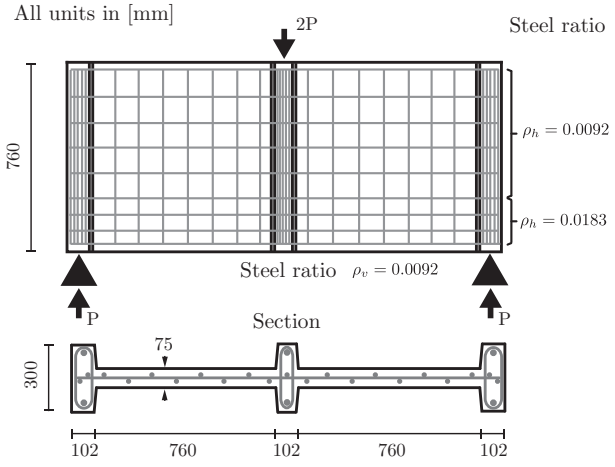

Fig. 12. Geometry and reinforcement details of the RC specimen W2.

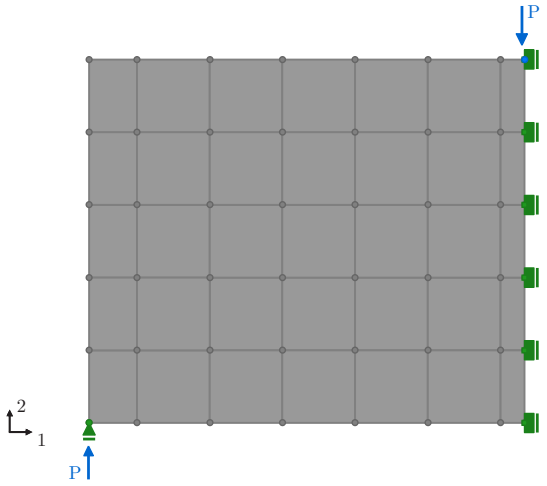

Fig. 13. Analytical model of the RC panel W2.

Es = 190,000 [MPa] (27,300 [ksi]), which was obtained from tensile tests of the bare bars [17]. The concrete in specimen W2 has a compression strength of $f'_c = 26.8$ [MPa] (3.88 [ksi]) after 15 days and a compression strain (ε_{c_0}) between −0.002 and −0.003 [mm/mm] [17].

The analytical model of the specimen was represented using only half of the specimen (only one panel) because of the symmetry of the specimen in geometry and loading. In addition, the test was modeled using a mesh of 150 [mm] by 150 [mm] (Fig. 13).

In addition, the analytical model was analyzed with and without considering the modification coefficients for the concrete model (softening and enhancement) to investigate the effects of these factors, which were compared with the load–displacement response that was obtained from the experimental results; see Figs. 14 and 15. The modification factors were not relevant in the case of a monotonic loading and could be ignored without any loss of accuracy.

Fig. 15 shows the response of the analytical model featuring quadrilateral membrane elements without drilling degrees of freedom (well-known bilinear field interpolation formulation) and the same factors, parameters and material model that were used in the model with the drilling DOF. A comparison of Figs. 15 and 14 shows that the elements without the drilling DOF were underestimated or overestimated, but these discrepancies were not significant compared with the results obtained for the model with the drilling DOF. However, in the elements with drilling DOF, fewer convergence problems for the same step size were observed, and in the models with convergence problems, the elements with drilling DOF were more than 15% faster than the model without drilling DOF.

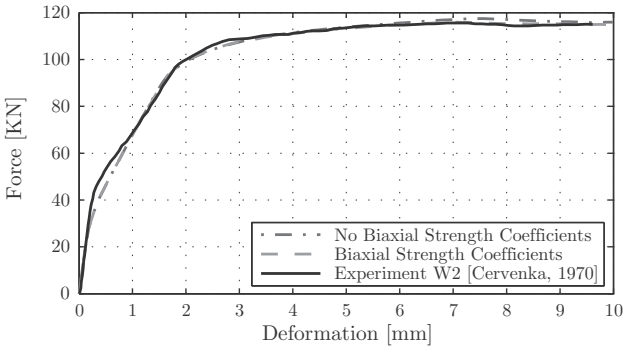

Fig. 14. Load-deformation of the response of the RC panel W2.

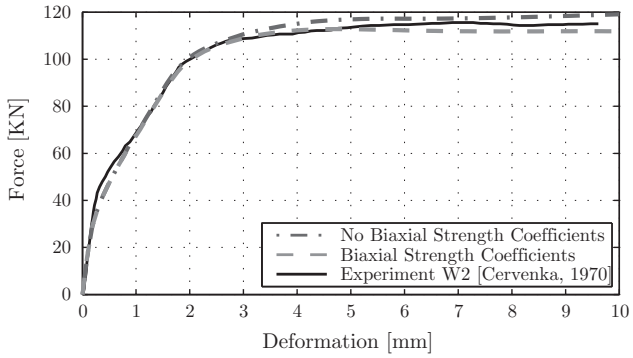

Fig. 15. Load-deformation of the response of the RC panel W2 using a quadrilateral layered membrane element without drilling degrees of freedom.

4.1.2. RC walls – Lefas, Kotsovos and Ambraseys

The study of Lefas et al. [63] in 1990 presented the results for a series of 13 walls that were submitted to a constant vertical load; a monotonic load was applied horizontally at the top of the wall specimen until wall failure occurred. The test program was conducted to study the effect of the axial load, height-to-width ratio, concrete strength and ratio of steel in the response of the walls with a rectangular cross-section [63]. The wall specimens were divided into two types: Type-I walls and Type-II walls, depending on their geometry (height-to-width ratio). Type-I walls correspond to specimens with a height-to-width ratio of $h/l = 1$ (750 [mm] wide × 750 [mm] high) and a thickness of 70 [mm] for the rectangular cross-section (see Fig. 16). Type-II walls correspond to specimens with a height-to-width ratio of $h/l = 2$ (650 [mm] wide × 1300 [mm] high) and a thickness of 65 [mm] for the rectangular cross-section; see Fig. 16. Three different sizes of steel bars were used as reinforcement in the walls; see Table 1 for the properties of the steel provided by Lefas et al. [63] in 1990.

In this study, three specimens of Type-I walls and three specimens of Type-II walls were used to compare the analytical results with the experimental results, and only information pertaining to these groups of specimens is mentioned here. In Table 2, the cube strength of the concrete and the ratio of reinforcement steel in each orientation for the specimens that were used in this study and provided by Lefas et al. [63] in 1990 are presented. These values were used to generate a model that converts cube strength to cylinder strength, which is typically defined as $f'_c = \alpha f'_{c\_cube}$, where α is a factor determined by the experimental data. This value lies between 0.77 (for low-strength concrete) and 0.95 (for high-strength concrete) [67].

The analytical model of Type-I and Type-II walls was performed using a mesh between 120 [mm] and 150 [mm] (Fig. 17).

In addition, as in the previous analysis, the analytical model that does not consider softening coefficients but uses the enhanced coefficient because of confinement at the boundary elements of the wall and the model that considers the softening and the enhanced coefficient because of confinement at the boundary elements of the wall were analyzed; see Figs. 18 and 20. Moreover, the experimental results were compared with the results yielded by the analytical model using a quadrilateral layered membrane element without drilling DOF; see Fig. 19.

These figures show that the model using the modification coefficients for the concrete better fit the experimental results for the top deformation of the wall, but as previously mentioned, the improvement achieved in using the coefficients is not significant

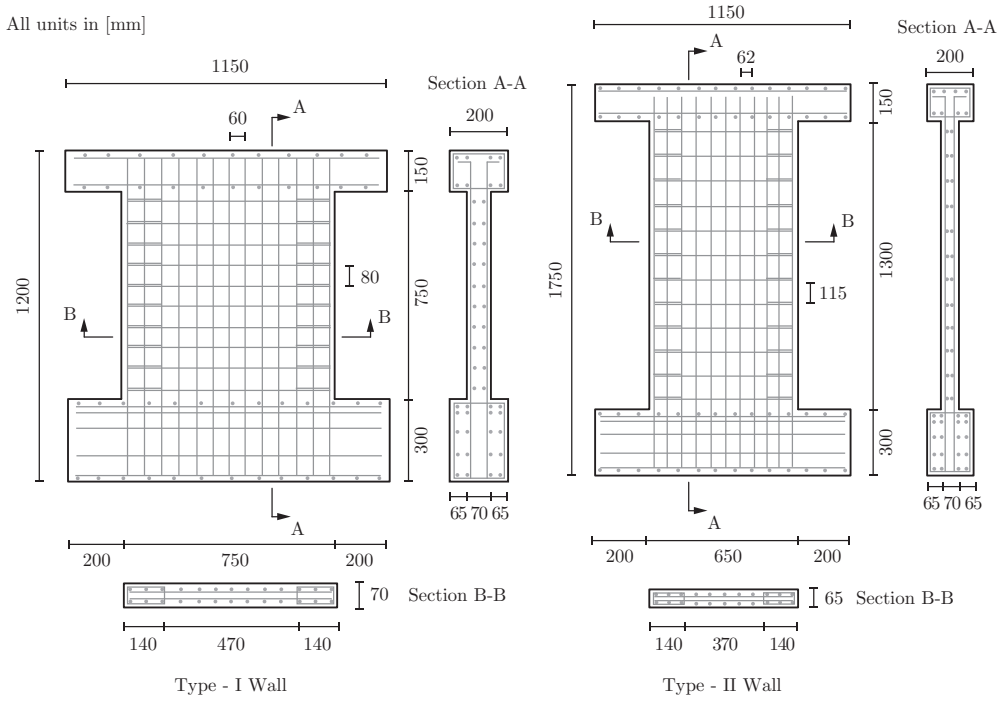

Fig. 16. Geometry and reinforcement details of Type-I and Type-II walls tested by Lefas et al. [63] in 1990.

Table 1
Properties of the reinforcement steel bars (after [63]).

Type	Yield strength (f_y) [MPa]	Ultimate strength (f_u) [MPa]
8 [mm] high-tensile bar (vertical reinf.)	470	565
6 [mm] high-tensile bar (horizontal reinf.)	520	610
4 [mm] mild steel bar (stirrups)	420	490

for Type-II wall. Additionally, the model featuring the quadrilateral layered membrane elements with drilling DOF better reflects the experimental results than the model with quadrilateral layered membrane elements without drilling DOF, but the difference is not significant for the monotonic cases. However, in the elements with drilling DOF, fewer convergence problems were observed for the same step size, and in the models with convergence problems, the elements with drilling DOF were more than 20% faster than the model without drilling DOF.

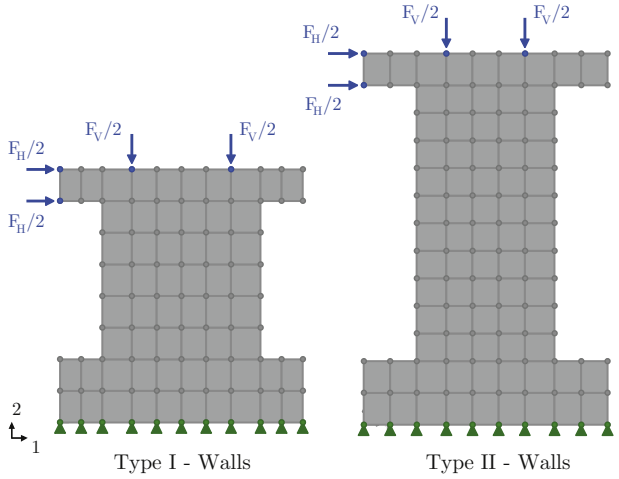

Fig. 17. Analytical model for Type-I and Type-II walls.

4.2. Reversal or cyclic loading

This section discusses how the proposed nonlinear layered quadrilateral membrane element with drilling degrees of freedom was evaluated and analyzed using the experimental test results under reversal loads. The selected test corresponds to the test program reported by Thomsen and Wallace [64] in 1995 and the tests

Table 2
Properties of the wall specimens (after [63]).

Type	Specimen	Steel ratio				Cube strength f'_{c_cube} [MPa]	Axial load	
		ρ_{hor} [%]	ρ_{ver} [%]	ρ_{flex} [%]	ρ_s [%]		F_v [KN]	$v = \frac{F_v}{blf'_c}$
I	SW11	1.10	2.40	3.10	1.20	52.3	0	0.0
	SW12	1.10	2.40	3.10	1.20	53.6	230	0.1
	SW16	1.10	2.40	3.10	1.20	51.7	460	0.2
II	SW22	0.80	2.50	3.30	0.90	50.6	182	0.1
	SW23	0.80	2.50	3.30	0.90	47.8	343	0.2
	SW24	01.80	2.50	3.30	0.90	48.3	0	0.0

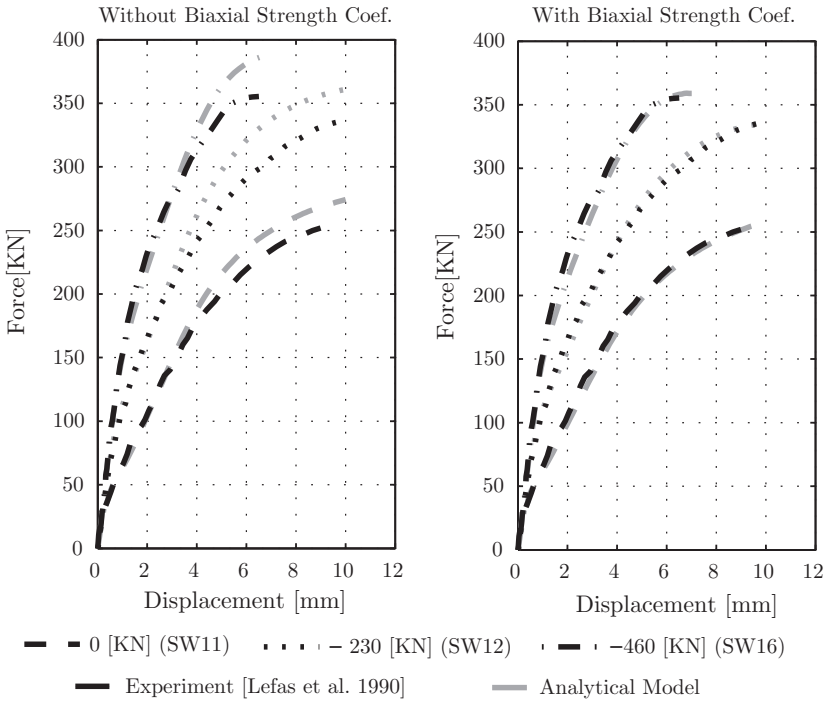

Fig. 18. Load–displacement curve of the analytical model versus the experiment results for Type-I walls.

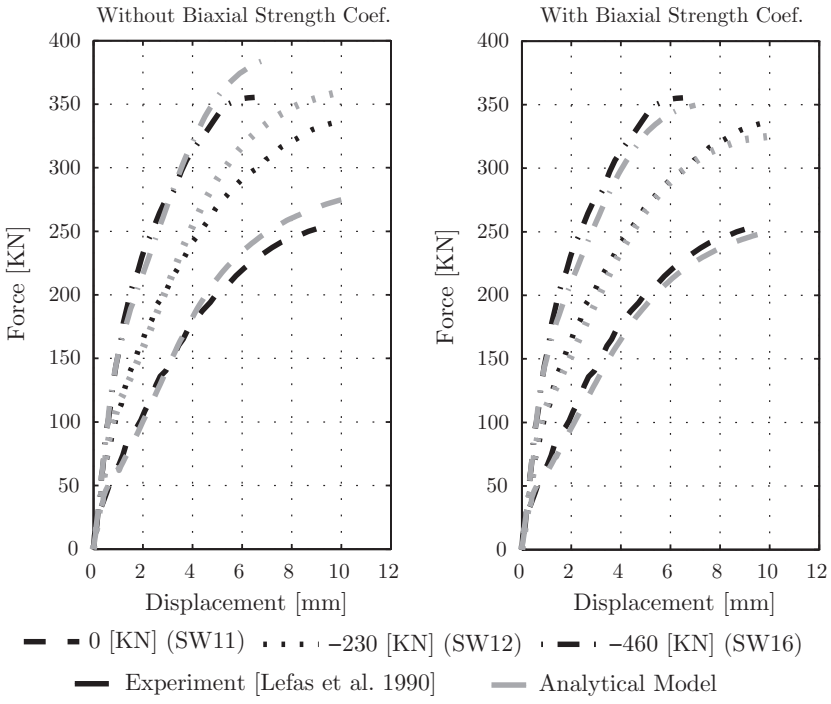

Fig. 19. Load–displacement curve of the analytical model with quadrilateral layered membrane elements without drilling DOF versus the experiment results for Type-I walls.

of reinforced concrete wall with irregulars disposition of openings conducted by Yañez [62] in 1993.

4.2.1. Reinforced concrete rectangular wall – Thomsen and Wallace

In the study performed by Thomsen and Wallace [64] in 1995, two rectangular-wall specimens (RW1 and RW2) measuring 1219 [mm] (48 [in]) long were used. These specimens were designed to approximately represent a one-quarter scale experimental model of a real wall that was designed using the Uniform Building Code of 1994 (UBC) [68] with additional boundary detailing in the reinforcement for the bottom part of the wall (the last 1219 mm or 48 [in] of the wall). The specimen walls were 3658 [mm] (144 [in]) tall with a thickness of 102 [mm] (4 [in]) over the entire cross-section of the specimens and were axially loaded with a value of

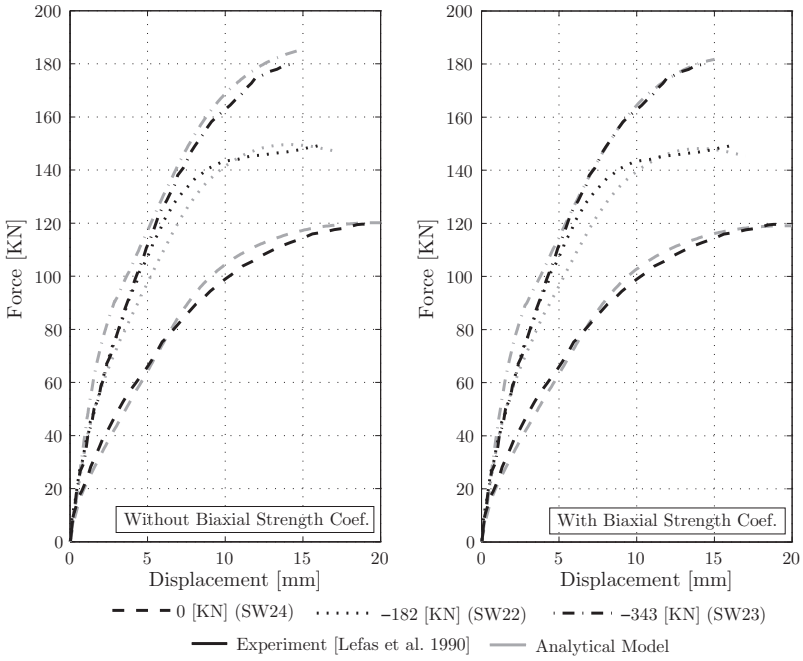

Fig. 20. Load–displacement curve of the analytical model versus the experiment results for Type-II walls.

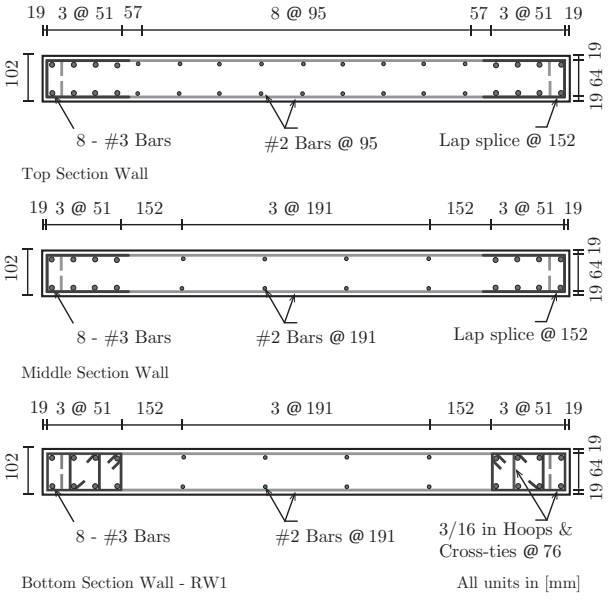

Fig. 21. Reinforcement details of specimen wall RW1, which was used by Thomsen and Wallace [64] in 1995.

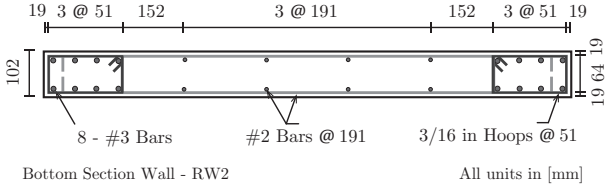

Fig. 22. Reinforcement details of specimen wall RW2, which was used by Thomsen and Wallace [64] in 1995.

Table 3
Properties of the reinforcement steel bars (after [64]).

Type	Yield Strength (f_y) [MPa]	Area$_b$ [mm^2]
No 3 – 9.53 [mm] bar	414	71
No 2 – 6.35 [mm] bar	448	32
3/16 in – 4.75 [mm] smooth wire	∽448	17.72

$\backsim 0.10 A_g f'_c$, after which they were cyclically loaded laterally, as reported by Thomsen and Wallace [64].

The steel ratio at each location in the wall was calculated based on the reinforcement details, which were provided in the report by Thomsen and Wallace [64]. Figs. 21 and 22 show the reinforcement details of the rectangular-wall specimens.

Table 3 presents the properties of the steel bars, which were provided in the report by Thomsen and Wallace [64].

The concrete of different wall specimens and at different levels of the wall was mixed to obtain a target value with a concrete strength of 27.6 [MPa] (4 [ksi]). However, different values of concrete strength were obtained for the different cylindrical tests that were performed on the concrete, and the values ranged from 28.7 to 58.4 [MPa] (4.16 to 8.46 [ksi]), as reported by Thomsen and Wallace [64], with an average value of 32.8 [MPa] (4.76 [ksi]) for specimen RW1 and an average value of 42.8 [MPa] (6.2 [ksi]) for RW2 [3].

The analytical model of the wall specimen was developed using a mesh of 170 [mm] (Fig. 23). In addition, the modification coefficient for damage because of cycling in the material was included in the model. The values of the peak strength of concrete, which were provided by Thomsen and Wallace [64], were used to generate the model.

Figs. 24 and 25 compare the responses of the analytical model and the experimental results of the load that was applied to the wall versus the deformation at the top of the wall for the two walls RW1 and RW2, using a damage coefficient (α_1) of 0.15. Additionally, Fig. 24 shows that the analytical model can capture the maximum capacity of the RW1 at the maximum displacement of approximately 80 [mm]. In RW1 ($s/d = 8$ where s: spacing hoops

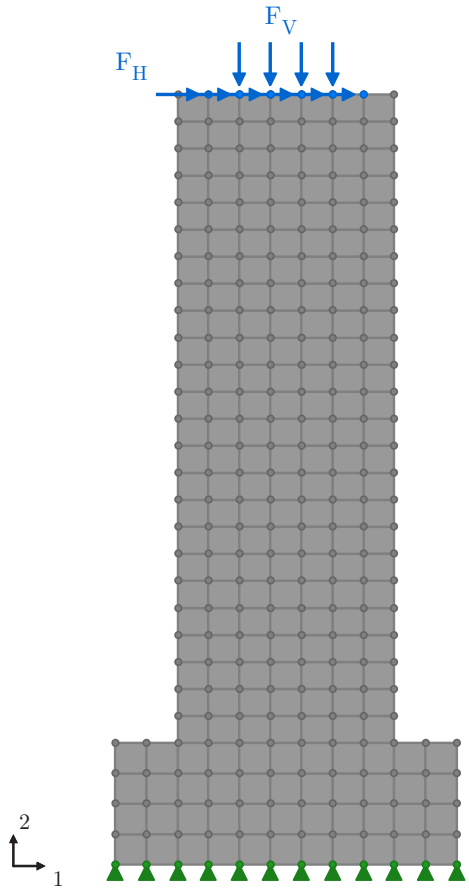

Fig. 23. Analytical model for rectangular-wall specimens (RW).

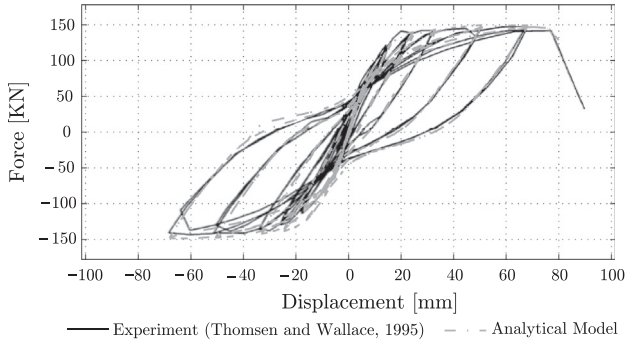

Fig. 24. Load–displacement curve of the analytical model versus the experiment results for RW1.

and *d*: diameter of longitudinal bar), the steel model with buckling was not included because it was observed that the use of this material does not produce a significant change in the response of the model.

In addition, the vertical strain along the wall, which was obtained using the experimental data from the instrument at the base of the walls (gauge length of 229 mm), was compared with that of the analytical model at the same base level for different drifts levels for RW2 (Fig. 26); the strain was obtained as the average of the strain observed in the model along the gauge length of 226 mm to match the quadrature points. Fig. 26 shows that the analytical data are consistent with the experimental data, which indicates that the formulation can predict both the global response and the local response observed in the wall.

4.2.2. Reinforced concrete wall with irregulars disposition of openings – Yañez

In 1993, Yañez [62] presented the results for a series of six three-story walls (one without an opening, two with regular disposition of openings and three with irregular disposition of openings). The specimens were scaled to one-third their original size and submitted to a cyclic lateral load applied to the top of the wall until failure of the specimens. The test program was conducted to study the effect of openings in reinforced concrete walls and the use of strut and tie methods for the analysis and design of this type of wall [62].

The walls correspond to specimens with a height-to-width ratio of $h/l = 1.25$ (2000 [mm] wide × 2300 [mm] high) and a thickness of 120 [mm] for the rectangular cross-section, with specimen S1 featuring no openings; specimens S2, S3 and S5 featuring openings measuring 600 [mm] by 600 [mm]; and specimens S4 and S6 featuring openings measuring 400 [mm] by 400 [mm]. The vertical and horizontal reinforcement ratio for the walls in all the specimens were 0.5% and 0.4 % respectively. The horizontal bars were spaced 180 mm and 100 mm apart ($s/d = 22.5$ and $s/d = 12.5$ where s: spacing of horizontal bars and hoops and d: diameter of longitudinal bar), the measured yield strength was 475 [MPa] at 0.2% strain and the ultimate strength was 690 [MPa] [62]. The reversed load was applied in two stages.

In this study, specimen S4 was used to compare the analytical results with the experimental results, and only information pertaining to this specimen is mentioned here. This specimen was selected because of the irregular disposition of the openings and the size of the openings (see Fig. 27), which make the model an interesting case study. In the columns of the specimen S4, the hoops were spaced 100 mm apart, increasing the horizontal reinforcement ratio in these areas. The yield strength and the ultimate

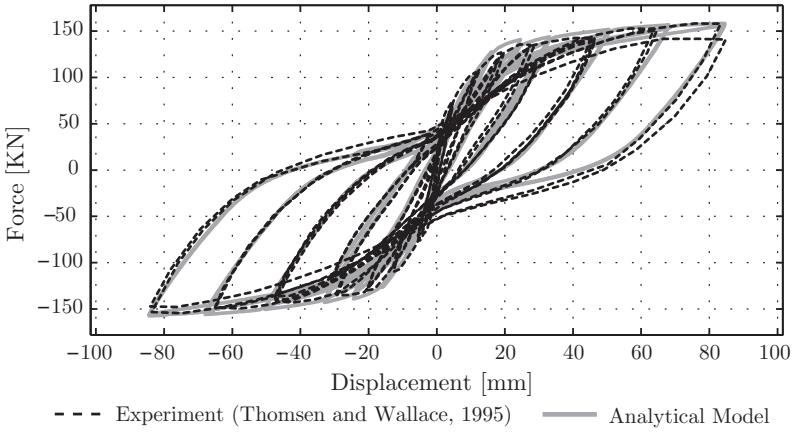

Fig. 25. Load–displacement curve of the analytical model versus the experiment results for RW2.

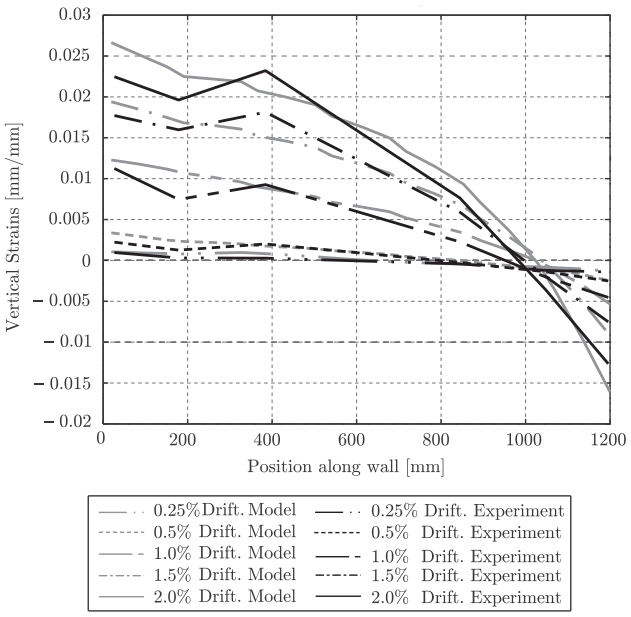

Fig. 26. Comparison of the vertical strain of the experimental data with the analytical model at the base level for RW2.

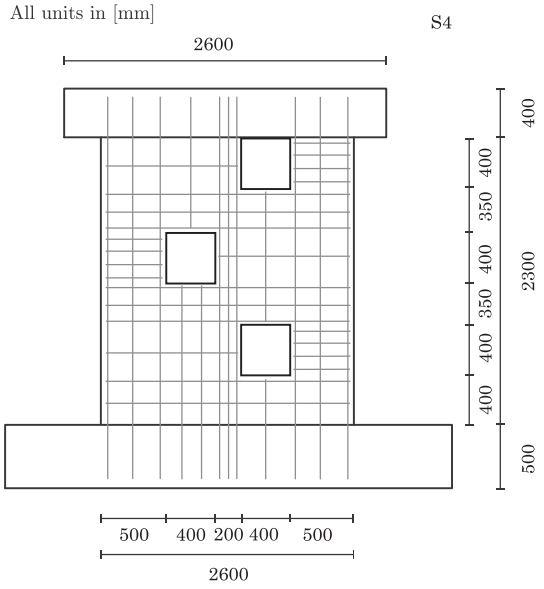

Fig. 27. Specimen S4 used by Yañez [62] in 1993.

strength of steel bars of the hoops were 350 [MPa] and 470 [MPa], respectively [62]. The concrete compressive cylinder strength at the moment of testing was 31 [MPa] for specimen S4 [62]. These values were used to generate the model. The specimen was modeled using a mesh of ~200 [mm] by ~200 [mm] (see Fig. 28). In this model, the steel model proposed by Massone and Moroder [60] in 2009 was used because the buckling behavior of the bar was necessary to correctly predict the experimental results and hysteretic loops (see Fig. 29). This characteristic was required because of the spacing of the horizontal bars in the wall ($s/d = 22.5$ and $s/d = 12.5$).

Fig. 29 compares the responses of the analytical model and the experimental results of the load that was applied to the wall versus the deformation at the top of the wall for the wall S4 using a damage coefficient (α_1) of 0.15.

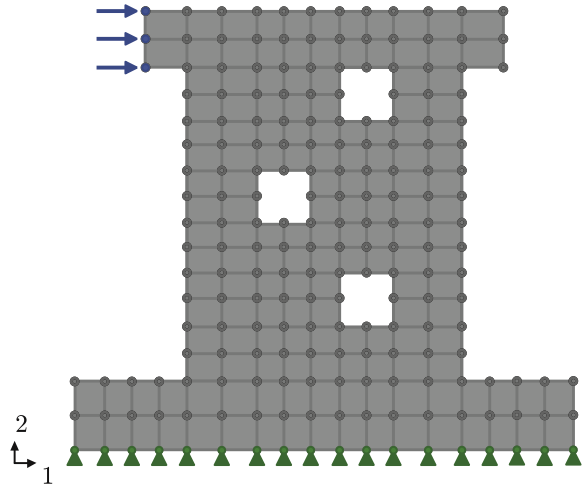

Fig. 28. Analytical model for the specimen S4.

In addition, the vertical strain along the wall, which was obtained based on the experimental data from the instrument (strain gauges) at the base of the walls, was compared with that of the analytical model at the same base level for 0.2%, 0.4% and 0.8% drift (Fig. 30), and the results show excellent agreement.

5. Conclusions

This paper presents a new element formulation for the nonlinear analysis of reinforced concrete (RC) walls under static and cycling loading. A general finite element formulation using a layered membrane element with drilling degrees of freedom was first presented. A layered section approach was used for each membrane or panel section, with separate constitutive models for the smeared concrete layer and smeared steel layer. These constitutive models were presented separately, which is different from other orthotropic models, such as the softened membrane model (SMM) or cyclic softened membrane model (CSMM) [69,28,29,70,71,35,36,19].

A variety of reported models using the material constitutive laws that represent the behavior of concrete were reviewed for this new formulation. Among the available models, the smeared crack approach using an orthotropic model with equivalent uniaxial average stress–strain relations along the axes of orthotropy was selected to represent the concrete plane stress behavior. This type of model shows outstanding accuracy, robustness and simplicity in representing concrete in two dimensions. The average uniaxial stress–strain relations were represented by the uniaxial concrete material models proposed by Massone et al. [12] in 2009 and extended here for cyclic loading. The concrete model also incorporated characteristics from the models created by a research group from the University of Houston, such as the CSMM presented by Zhong [19] in 2005, and models created by a research group from the University of Toronto, such as the expanded MCFT developed by Palermo [43] in 2002 and Palermo and Vecchio [33] in 2003 and the concrete model presented by Vecchio [44] in 1992. Other additional characteristics were incorporated to consider the effect of biaxial compression or tension–compression (softening) along the axes of orthotropy and account for damage in the material during cyclic loading and enhancement due to confinement.

The smeared steel constitutive material used to represent the horizontal and vertical reinforcement steel layers in the membrane element was also presented. In this approach, the steel bars were assumed to be a layer of homogeneous material at certain positions inside the reinforced concrete element, and the stress variation due to cracking over an area could be modeled using the average

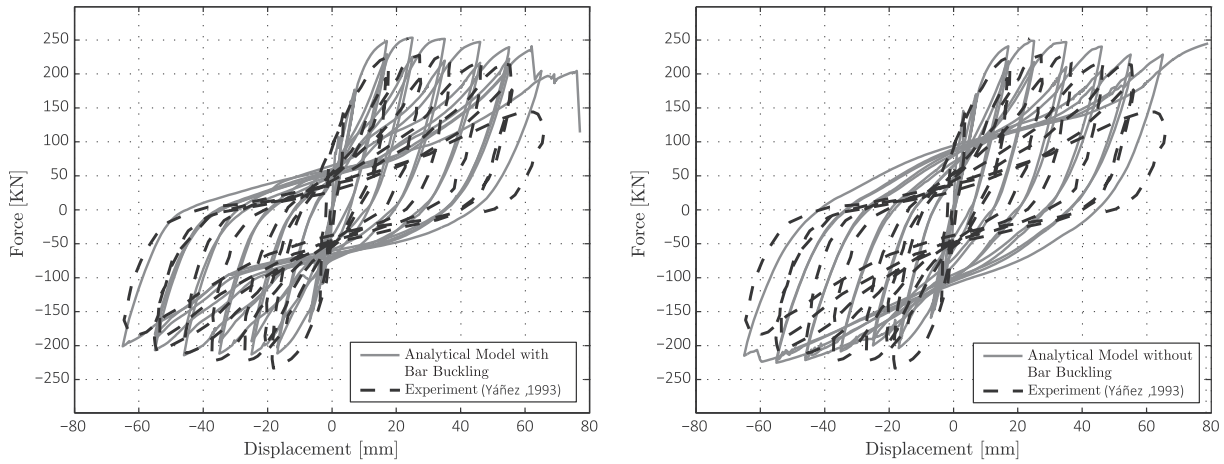

Fig. 29. Load–displacement curve of the analytical model (with and without bar buckling) versus the experiment results for S4.

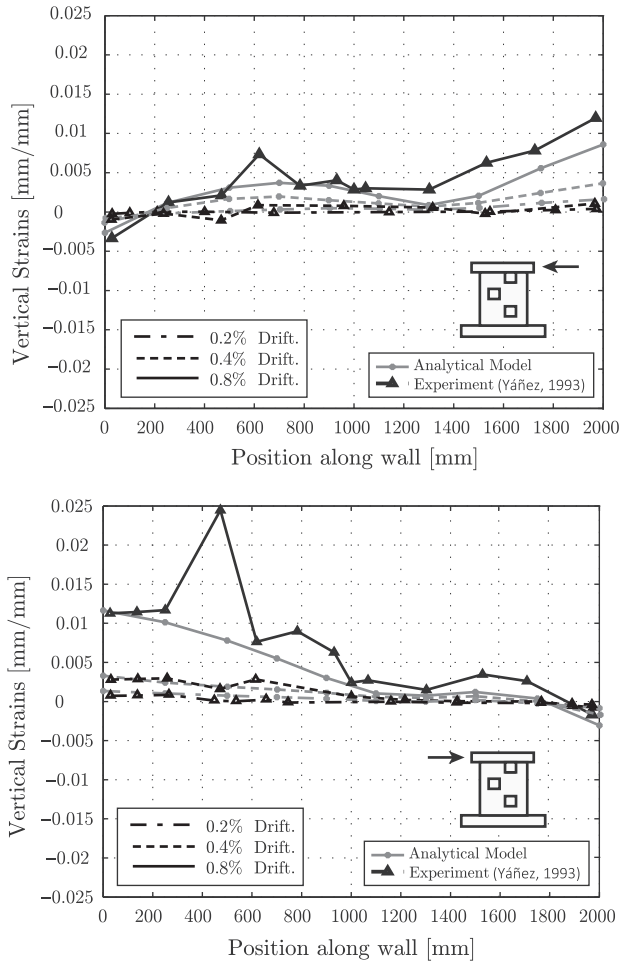

Fig. 30. Comparison of the vertical strain at the base level of the experimental data with the analytical model including bar buckling for S4.

stress–strain of steel in that zone. It was also assumed that the smeared steel worked only in the direction of the bar because the bars were typically in a uniaxial state of stress, allowing for the use of a uniaxial constitutive model. Two uniaxial steel material models were used: the well-known Menegotto–Pinto steel model proposed by Menegotto and Pinto [59] in 1973 and the model proposed by Massone and Moroder [60] in 2009, which includes buckling behavior.

The different features of the proposed model were selected with the goal of using the developed layered section approach and to obtain a numerically stable, reliable and efficient constitutive material.

The last section of this article discusses how the accuracy, applicability, and usefulness of the proposed nonlinear layered quadrilateral membrane with drilling degrees of freedom were evaluated. To verify the analytical model, a set of experiment results for RC wall elements under monotonic and reversed loads, which are available in the literature, was used. The selected tests have also been used as benchmarks by other authors.

The experimental results can be divided into those pertaining to monotonic loading and those pertaining to reversed loading. For monotonic loading, two different experiments were used. The tests for monotonic loading were selected to confirm that the model is able to capture the capacity and stiffness of different configurations of walls under this type of loading and to compare the responses of a model with and without DOFs. The first experiment considered one of the experimental results from the wall tests conducted by Cervenka and Gerstle and presented in Cervenka [17] in 1970, which correspond to a squat wall. The model was able to correctly predict the global behavior of the wall. The second set of tests considered the experimental results of two types of walls with different aspect ratios, which were reported by Lefas et al. [63] in 1990; the model was able to correctly predict the capacity and the global response of the wall for the two aspect ratios studied. In addition, these analyses showed that the use of biaxial compression or tension–compression (softening) along the axes of orthotropy is only relevant under monotonic loading for elements whose principal behavior is shear, and not for elements whose principal behavior is flexural.

For reversal or cyclic loading, the test results obtained for two rectangular single walls obtained by Thomsen and Wallace [64] in 1995 and the experimental results obtained for a reinforced concrete wall with irregular disposition of openings obtained by Yañez [62] in 1993 were compared. The comparison showed that the analytical model can correctly predict the load vs displacement curves for the walls RW1 and RW2. Additionally, the analytical model can match the observed maximum capacity of RW1 and the ductile behavior of the better confined rectangular wall RW2, produced for the different amounts of reinforcement placed on the two walls. The model is also able to reproduce the local behavior of the wall at different drift levels. In addition, the model, which includes buckling behavior, obtained good agreement between the complete global and local behavior for a complex wall with an irregular distribution of openings (S4 specimen).

In conclusion, the presented formulation, which uses a nonlinear layered quadrilateral membrane element with drilling degrees of freedom, can predict the maximum capacity, the global and the local response observed in RC walls with different configurations (wall size, ratio of steel, and concrete strength). In addition, the formulation could be used as the basis for creating a shell element with layered sections to model 3D RC walls.

Acknowledgments

We would like to thank graduate student Sebastian Albornoz for contributing to the implementation of the models of walls with irregular disposition of openings.

References

[1] Paulay T, Priestley MJN. Seismic design of reinforced concrete and masonry buildings. John Wiley and Sons, Inc; 1992.
[2] Bertero VV. Seismic behaviors of rc wall structural system. 7th World conference on earthquake engineering, vol. 6. p. 323–30. Instalbul, Turkey.
[3] Orakcal K, Massone LM, Wallace JW. Analytical modeling of reinforced concrete walls for predicting flexural and coupled-shear-flexural responses. PEER report 2006/07. Los Angeles: Pacific Earthquake Engineering Research Center, University of California; 2006.
[4] Eimani T. Analytical model for reinforced concrete shear wall structures Phd dissertation. Los Angeles, California: University of Southern California; 1997.
[5] Naeim F, Lew M, Carpenter LD, Youssef NF, Rojas F, Saragoni GR, et al. Performance of tall buildings in santiago, chile during the 27 february 2010 offshore maule, Chile earthquake. Struct Des Tall Special Build 2011;20 (1):1–16.
[6] Youssef NF, Tunick D, Naeim F, Lew M, Carpenter LD, Rojas F, et al. Performance of the torre bosquemar and olas buildings in san pedro de la paz and the pedro de valdivia building in concepción in the 27 february 2010 offshore maule, Chile earthquake. Struct Des Tall Special Build 2011;20(1):65–82.
[7] Carpenter LD, Naeim F, Lew M, Youssef NF, Rojas F, Saragoni GR, et al. Performance of tall buildings in viña del mar in the 27 february 2010 offshore maule, Chile earthquake. Struct Des Tall Special Build 2011;20(1):17–36.
[8] Rojas F, Naeim F, Lew M, Carpenter LD, Youssef NF, Saragoni GR, et al. Performance of tall buildings in concepción during the 27 february 2010 moment magnitude 8.8 offshore maule, Chile earthquake. Struct Des Tall Special Build 2011;20(1):37–64.
[9] Moehle J, Wallace JW, Maffei J, Sempere C, Celestino A, Besa JJ, et al. February 27, 2010 chile earthquake reconnaissance team investigation: reinforced concrete buildings. Reconnaissance report, EERI; 2010.
[10] Vulcano A, Bertero VV. Analytical models for predicting the lateral response of rc shear walls: evaluation of their reliability. UCB/EERC 87/19. Earthquake Engineering Research Center, University of California, Berkeley; 1987.
[11] Kabeyesawa TH, Shiohara S, Otani S, Aoyama H. Analysis of the full-scale 7-story r.c. test structure. In: 3rd Joint technical coordinating committee, U.S Japan cooperative earthquake research program. Tsukuba: Building Research Institute; 1982.
[12] Massone LM, Orakcal K, Wallace JW. Modeling of squat structural walls controlled by shear. ACI Struct J 2009;105(5):646–55.
[13] Jiang H, Kurama Y. Analytical modeling of medium-rise reinforced concrete shear walls. ACI Struct J 2010;107(4):400–10.
[14] Panagiotou M, Restrepo JI, Schoettler M, Kim G. Nonlinear cyclic truss model for reinforced concrete walls. ACI Struct J 2012;109(2):205–14.
[15] Kolozvari K, Orakcal K, Wallace J. Modeling of cyclic shear-flexure interaction in reinforced concrete structural walls. i: Theory. J Struct Eng 2015;141(5).
[16] Chen WF. Plasticity in reinforced concrete. Reprint ed. 5765 N Andrews Way, Fort Lauderdale: J Ross Publishing Classic; 2007.
[17] Cervenka V. Inelastic finite element analysis of reinforced concrete panels under in-plane loads Phd thesis. Boulder, Colorado: University of Colorado; 1970.
[18] Ayoub A, Filippou FC. Nonlinear finite-element analysis of rc shear panels and walls. J Struct Eng 1998;124(3):298–308.
[19] Zhong J. Model-based simulation of reinforced concrete plane stress structures Phd dissertation. Houston, United States: Department of Civil and Environmental Engineering, University of Houston; 2005.
[20] Darwin D, Pecknold DAW. Inelastic model for cyclic biaxial loading of reinforced concrete. Civil engineering studies, structural research series 409. Urbana, Illinois, United States: University of Illinois at Urbana-Champaign; 1974.
[21] Darwin D, Pecknold DA. Analysis of cyclic loading of plane structures. Comput Struct 1977;7(1):137–47.
[22] Cervenka V. Constitutive model for cracked reinforced concrete. ACI J 1985;82 (6):877–82.
[23] Vecchio FJ, Collins MP. The modified compression-field theory for reinforced concrete elements subjected to shear. ACI J Proc 1986;83(2):219–31.
[24] Izumo J, Shin H, Maekawa K, Okamura H. An analytical model for rc panels subjected to in-plane stresses. In: International workshop on concrete shear earthquake. Houston: Elsevier Science Publishers, Inc; 1991. p. 206–15.
[25] Shin H, Maekawa K, Okamura H. Analytical models for reinforced concrete shear walls under reversal cyclic loading. In: International workshop on concrete shear earthquake. Houston: Elsevier Science Publishers, Inc; 1991. p. 289–98.
[26] Bolander JJ, Wight JK. Finite element modeling of shear-wall-dominant buildings. J Struct Eng 1991;117(6):1719–39.
[27] Hsu TTC. Nonlinear analysis of concrete membrane elements. ACI Struct J 1991;88(5):552–61.
[28] Belarbi A, Hsu TTC. Constitutive laws of softened concrete in biaxial tension compression. ACI Struct J 1995;92(5):562–73.
[29] Pang XBD, Hsu TTC. Behavior of reinforced concrete membrane elements in shear. ACI Struct J 1995;92(6):665–79.
[30] Pang XBD, Hsu TTC. Fixed angle softened truss model for reinforced concrete. ACI Struct J 1996;93(2):196–208.
[31] Vecchio FJ. Disturbed stress field model for reinforced concrete: formulation. J Struct Eng 2000;126(9):1070–7.
[32] Vecchio FJ. Disturbed stress field model for reinforced concrete: implementation. J Struct Eng 2001;127(1):12–20.
[33] Palermo D, Vecchio FJ. Compression field modeling of reinforced concrete subjected to reversed loading: formulation. ACI Struct J 2003;100(5):616–25.
[34] Foster SJ, Marti P. Cracked membrane model: finite element implementation. J Struct Eng 2003;129(9):1155–63.
[35] Mansour M, Hsu TTC. Behavior of reinforced concrete elements under cyclic shear. i: Experiments. J Struct Eng 2005;131(1):44–53.
[36] Mansour M, Hsu TTC. Behavior of reinforced concrete elements under cyclic shear. ii: Theoretical model. J Struct Eng 2005;131(1):54–65.
[37] Bathe KJ. Finite elements procedures. Upper Saddle River, New Jersey 07458: Prentice Hall, Inc.; 1996.
[38] Cook RD, Malkus DS, Plesha ME, Witt RJ. Concepts and applications of finite element analysis. 4th ed. John Wiley & Sons, Inc; 2002.
[39] Zhang YX, Bradford MA, Gilbert RI. A layered shear-flexural plate/shell element using timoshenko beam functions for nonlinear analysis of reinforced concrete plates. Finite Elem Anal Des 2007;43(11–12):888–900.
[40] Zhang YX, Bradford MA, Gilbert RI. A layered cylindrical quadrilateral shell element for nonlinear analysis of rc plate structures. Adv Eng Softw 2007;38 (7):488–500.
[41] Xia G, Yu M, Li C, Zhang J. Rectangular membrane element with rotational degree of freedom. In: Procedings of the international symposium on computational structural engineering. Shanghai, China. p. 1051–8.
[42] Rojas F. Development of a nonlinear quadrilateral layered membrane element with drilling degrees of freedom and a nonlinear quadrilateral thin flat layered shell element for the modeling of reinforced concrete walls Phd dissertation. Los Angeles, California: University of Southern California; 2012.
[43] Palermo D. Behavior and analysis of reinforced concrete walls subjected to reversed cycling loading Phd thesis. Toronto, Canada: Department of Civil Engineering, University of Toronto; 2002.
[44] Vecchio FJ. Finite element modeling of concrete expansion and confinement. J Struct Eng 1992;118(9):2390–406.
[45] Crisfield MA, Wills J. Analysis of r/c panels using different concrete models. J Eng Mech, ASCE 1989;115(3):578–97.
[46] Thorenfeldt E, Tomaszewicz A, Jensen JJ. Mechanical properties of high-strength concrete and application in design. In: Symposium utilization of high-strength concrete. Stavanger, Norway.
[47] Popovics S. A numerical approach to the complete stress-strain curve of concrete. Cem Concr Res 1973;3(5):583–99.
[48] Collins MP, Porasz A. Shear strength for high strength concrete. chap. Bulletin D'Information No. 193 – design aspects of high strength concrete. Paris, France; 1989. p. 75–83.
[49] Polak MA, Vecchio FJ. Nonlinear analysis of reinforced-concrete shells. J Struct Eng 1993;119(12):3439–62.
[50] Vecchio FJ, Collins MP. Compression response of cracked reinforced concrete. J Struct Eng 1993;119(12):3590–610.
[51] Carreira DJ, Kuang-Han C. Stress–strain relationship for plain concrete in compression. ACI Struct J 1985;82(6):797–804.
[52] Belarbi A, Hsu TTC. Constitutive laws of concrete in tension and reinforcing bars stiffened by concrete. ACI Struct J 1994;91(4):465–74.
[53] Tamai S, Shima H, Izumo J, Okamura H. Average stress–strain relationship in post-yield range of steel bar in concrete. Concrete library of JSCE, translation of proceedings of JSCE, vol. 378(6). p. 117–29.
[54] Mohd Yassin MH. Nonlinear analysis of prestressed concrete structures under monotonic and cyclic loads Phd dissertation. Berkeley; Berkeley, California: University of California; 1994.
[55] Mansour M, Lee JY, Hsu TTC. Cyclic stress–strain curves of concrete and steel bars in membrane elements. J Struct Eng 2001;127(12):1402–11.
[56] Powanusorn S. Effect of confinement on shear dominated reinforced concrete elements Ph.D. thesis. Texas: Texas A&M University; 2003.
[57] Kupfer H, Hilsdorf H, Rusch H. Behavior of concrete under biaxial stresses. ACI J 1969;66(8):656–66.
[58] Mander JB, Priestley JN, Park R. Theoretical stress–strain model for confined concrete. J Struct Eng 1988;114(8):1804–26.
[59] Menegotto M, Pinto PE. Method of analysis of cyclically loaded reinforced concrete plane frames including changes in geometry and non-elastic behavior of elements under combined normal force and bending. In: IABSE symposium

on the resistance and ultimate deformability of structures acted on by well-defined repeated loads. Lisbon.
[60] Massone LM, Moroder D. Buckling modeling of reinforcing bars with imperfections. Eng Struct 2009;31(3):758–67.
[61] Filippou FC, Popov EG, Bertero VV. Effects of bond deterioration on hysteretic behavior of reinforced concrete joints. UCB/EERC 83/19, Earthquake Engineering Research Center. Berkele: University of California; 1983.
[62] Yañez F. Seismic behaviour of r.c. walls with irregular openings Phd dissertation. Canterbury, New Zealand: University of Canterbury; 1993.
[63] Lefas ID, Kotsovos MD, Ambraseys NN. Behavior of reinforced concrete structural walls: strength, deformation characteristic, and failure mechanism. ACI Struct J 1990;87(1):23–31.
[64] Thomsen JHI, Wallace JW. Displacement-based design of reinforced concrete structural walls: an experimental investigation of walls with rectangular and t-shaped cross sections. Report No. CU/CE-95-06. Clarkson University; 1995.
[65] Batoz JL, Dhatt G. Incremental displacement algorithms for nonlinear problems. Int J Numer Methods Eng 1979;14(8):1262–7.
[66] Vecchio FJ. Reinforced concrete membrane element formulations. J Struct Eng 1990;116(3):730–50.
[67] Mindess S, Young JF, Darwin D. Concrete. 2nd ed. Upper Saddle River, NJ 07458: Prentice Hall, Pearson Education, Inc.; 2003.
[68] Uniform Building Code (1994). International conference of building officials. Whittier, California; 1994.
[69] Hsu TTC. Unified theory of reinforced concrete. Boca Raton, Fl: CRC Press Inc.; 1992.
[70] Hsu TTC, Zhang LX. Nonlinear analysis of membrane elements by fixed-angle softened-truss model. ACI Struct J 1997;94(5):483–92.
[71] Hsu TTC, Zhu RRH. Softened membrane model for reinforced concrete elements in shear. ACI Struct J 2002;99(4):460–9.